NeuroImage 207 (2020) 116348

Contents lists available at ScienceDirect

NeuroImage

journal homepage: www.elsevier.com/locate/neuroimage

Investigating microstructural variation in the human hippocampus using non-negative matrix factorization

Raihaan Patel [a,b,*], Christopher J. Steele [a,c,d], Anthony G.X. Chen [a,e], Sejal Patel [a,f,g], Gabriel A. Devenyi [a,h], Jürgen Germann [a,i], Christine L. Tardif [b,j,k], M. Mallar Chakravarty [a,b,h,**]

[a] Cerebral Imaging Centre, Douglas Mental Health University Institute, Verdun, Canada
[b] Department of Biological and Biomedical Engineering, McGill University, Montreal, Canada
[c] Department of Psychology, Concordia University, Montreal, Quebec, H4B 1R6, Canada
[d] Department of Neurology, Max Planck Institute for Human Cognitive and Brain Sciences, Leipzig, Germany
[e] School of Computer Science, McGill University, Montreal, Canada
[f] Campbell Family Mental Health Research Institute, Centre for Addiction and Mental Health, Toronto, Canada
[g] Institute of Medical Science, University of Toronto, Toronto, Canada
[h] Department of Psychiatry, McGill University, Montreal, Canada
[i] University Health Network, Toronto, Canada
[j] McConnell Brain Imaging Centre, Montreal Neurological Institute, Montreal, Canada
[k] Department of Neurology and Neurosurgery, McGill University, Montreal, Canada

ARTICLE INFO

Keywords:
Hippocampus
Microstructure
MRI
Multimodal
Non-negative matrix factorization

ABSTRACT

In this work we use non-negative matrix factorization to identify patterns of microstructural variance in the human hippocampus. We utilize high-resolution structural and diffusion magnetic resonance imaging data from the Human Connectome Project to query hippocampus microstructure on a multivariate, voxelwise basis. Application of non-negative matrix factorization identifies spatial components (clusters of voxels sharing similar covariance patterns), as well as subject weightings (individual variance across hippocampus microstructure). By assessing the stability of spatial components as well as the accuracy of factorization, we identified 4 distinct microstructural components. Furthermore, we quantified the benefit of using multiple microstructural metrics by demonstrating that using three microstructural metrics (T1-weighted/T2-weighted signal, mean diffusivity and fractional anisotropy) produced more stable spatial components than when assessing metrics individually. Finally, we related individual subject weightings to demographic and behavioural measures using a partial least squares analysis. Through this approach we identified interpretable relationships between hippocampus microstructure and demographic and behavioural measures. Taken together, our work suggests non-negative matrix factorization as a spatially specific analytical approach for neuroimaging studies and advocates for the use of multiple metrics for data-driven component analyses.

1. Introduction

The hippocampus is a medial temporal lobe structure of the brain intimately linked with learning and memory. It is often described as a curved cylindrical structure with a tapered tail, spanning the anterior-posterior extent of the medial temporal lobe (Amaral, Scharfman and Lavenex, 2007; Small, 2002; Strange et al., 2014). Variation in hippocampal function, anatomy, and degeneration have been implicated in a variety of neurological disorders, including but not limited to Alzheimer's Disease (Amaral et al., 2018; Braak and Braak, 1991; Sabuncu et al., 2011), schizophrenia (Heckers, 2001; Narr et al., 2004), and depression (Bremner et al., 2000; Vythilingam et al., 2004). As a result, examination of this structure has consistently been of significant interest, particularly in the context of neuroimaging investigations. Structural magnetic resonance imaging (MRI)-based studies typically investigate the volume and shape of the hippocampus in relation to neuropsychiatric disorders and cognitive function (Bremner et al., 2000; Crane and Milner, 2005; de Flores et al., 2015; Erickson et al., 2011; Fotuhi et al., 2012;

* Corresponding author. Cerebral Imaging Centre, Douglas Mental Health University Institute, Verdun, Canada.
** Corresponding author. Cerebral Imaging Centre, Douglas Mental Health University Institute, Verdun, Canada.
E-mail addresses: mohammed.patel@mail.mcgill.ca (R. Patel), mallar@cobralab.ca (M.M. Chakravarty).

https://doi.org/10.1016/j.neuroimage.2019.116348
Received 26 August 2019; Received in revised form 5 November 2019; Accepted 8 November 2019
Available online 9 November 2019
1053-8119/© 2019 Elsevier Inc. This is an open access article under the CC BY-NC-ND license (http://creativecommons.org/licenses/by-nc-nd/4.0/).

Jack et al., 1999; Mielke et al., 2012; Sankar et al., 2017; Voineskos et al., 2015; Vythilingam et al., 2004).

While these studies are undoubtedly important and effective, they are limited by their ability to effectively probe the variance in overall architecture of the hippocampus, a heterogeneous structure with distinct subregions. To address concerns regarding the lack of spatial specificity in traditional hippocampal volume estimates, previous work has attempted to refine volumetric studies using subfield volumes (Amaral et al., 2018; Khan et al., 2008; Small et al., 2011; Winterburn et al., 2013; Wisse et al., 2014; Yushkevich et al., 2010). While this has proven to be useful in several studies (Adler et al., 2018; de Flores et al., 2015; Small et al., 2011; Voineskos et al., 2015; Yushkevich et al., 2015b), it still relies on *a priori* definitions of a specific type of hippocampal architecture that may be difficult to fully resolve using standard structural MRI techniques. For example, parts of the cornu ammonis region may have thickness under 1 mm (Amunts et al., 2005), and boundaries between the cornu ammonis 1 and subiculum are still a topic of controversy (Yushkevich et al., 2015a). Furthermore, inter- and intra-subfield variation based on well-characterized variation in genetics, function, and anatomical connectivity patterns along the hippocampal long axis can also be expected (Patel et al., 2017; Small, 2002; Strange et al., 2014; Thompson et al., 2008; Whelan et al., 2016). A goal of this work is to investigate the hippocampus using an approach which better captures the demonstrated intra-hippocampal variation.

Volumetric analyses also fail to describe hippocampus microstructure (defined here as alterations in tissue microstructure as described by MRI accessible measures). Given the relative lack of microstructural analyses of the hippocampus, a goal of the current manuscript is to examine the hippocampus along microstructural dimensions. Previous studies have used indices derived from diffusion MRI and/or quantitative MRI to demonstrate that microstructural variation throughout the brain can be reliably detected prior to volumetric change (Bartzokis, 2004; Callaghan et al., 2014; Lebel et al., 2012; Lebel et al., 2008; Marner et al., 2003) and in some cases may be more robustly related to variation in cognitive performance (Charlton et al., 2006; Charlton et al., 2010; den Heijer et al., 2012; Schiavone et al., 2009; Scott et al., 2017). These associations have also been demonstrated in the hippocampus specifically, and further motivate the investigation of hippocampal microstructure presented in the current manuscript (Carlesimo et al., 2010; den Heijer et al., 2012; Müller et al., 2007; van Uden et al., 2016; Wolf et al., 2015). Previous microstructural-based works have commonly focussed on the use of diffusion MRI derived metrics such as fractional anisotropy (FA) and mean diffusivity (MD) to describe axon geometry/organization and axon density (Alexander et al., 2007; Jones et al., 2013; Tardif et al., 2016). In addition to this, recent works have begun to use measures derived using structural MRI, specifically the ratio of T1-weighted/T2-weighted (T1w/T2w) signal as a correlate of myelin (Ganzetti et al., 2014; Glasser et al., 2016; Glasser and Van Essen, 2011; Grydeland et al., 2013; Tullo et al., 2019), as a means of further interrogating brain microstructural characteristics and their relationship with cognition (Grydeland et al., 2013) or age (Tullo et al., 2019). While each metric aims to assess different aspects of brain microstructure, none of them can be said to be specific to alterations of any unique biological phenomena (Alexander et al., 2007; Tardif et al., 2016). There also exists overlap in the phenomena to which each is sensitive (e.g. T1w/T2w, MD and FA are all sensitive to myelin content (Alexander et al., 2007; Grydeland et al., 2013; Tardif et al., 2016)). Thus, multivariate methods which assess multiple microstructural metrics simultaneously should offer more insight, and it is conceivable that the variation in cognition may be related to variation across microstructural indices and may not be uniquely attributable to a specific index. Therefore, another goal of this work is to explore the benefits of using multiple microstructural metrics simultaneously.

Combining metrics from multiple modalities requires the use of multivariate techniques. Within neuroimaging, techniques such as principal component analysis (PCA) and independent component analysis (ICA) are common choices (Arbabshirani et al., 2017; Beckmann and Smith, 2005; Beckmann, DeLuca, Devlin and Smith, 2005; Calhoun et al., 2001). These techniques are typically applied in a data-driven, exploratory fashion to identify dominant modes of variance in a given dataset (Hansen et al., 1999). They can be limited, however, by outputs which are difficult to interpret (Sotiras et al., 2015), due to the presence of positive and negative valued component weightings. More recently, neuroimaging studies have explored the use of non-negative matrix factorization (NMF) (Lee and Seung, 1999; Nassar et al., 2018; Sotiras et al., 2015; Thompson et al., 2008). Similar in some respects to standard PCA or ICA, NMF decomposes a single input matrix into two matrices whose product is an approximation of the original input. As described by its name, the unique feature of NMF is a non-negative constraint, abolishing negative output weightings. In the specific context of matrix decomposition, this allows a purely additive reconstruction and the ability to describe data as a sum of its parts. Thus, when interpreting components and assigning features to brain regions, while similar conclusions may be obtained without a non negativity constraint, NMF may allow more straightforward interpretation by removing the need to cancel out effects of opposing direction. Importantly, NMF has been shown to capture spatially contiguous and sensible patterns of genetic (Thompson et al., 2008) and neuroanatomical (Sotiras et al., 2015) variation.

In this work, we investigate MRI-accessible indices of microstructure in the human hippocampus at the voxel level using multimodal and multivariate approaches. Investigation at the voxel level allows us to remain sensitive to intra- and inter-subfield level variation and combining multiple modalities offers increased sensitivity and the potential for improved representations of complex neuroanatomical processes (Alexander et al., 2007; Tardif et al., 2016). Recent works have capitalized on multiple modalities for a range of applications, including cortical parcellation (Glasser et al., 2016), multifactorial modelling of Alzheimer's pathology (Iturria-Medina et al., 2017), and predicting an individual's 'brain age' (Liem et al., 2017). In the current work, we aim to define a normative microstructural parcellation of the hippocampus using NMF, a decomposition technique particularly suited to neuroimaging data due to its non negativity constraint. We also aim to assess the benefit of using multiple microstructural metrics by comparing the stability of microstructural parcellations using multiple metrics and a single metric. Finally, we aimed to relate individual variation in microstructural patterns to variation in cognitive performance using behavioural partial least squares analysis.

2. Methods

2.1. Overview

A subset of unrelated subjects from the Human Connectome Project were selected for analysis (2.2 Data). Hippocampus segmentations were obtained using the Multiple Automatically Generated Templates (MAGeT) Brain algorithm. T1w and T2w images were used to create a population average, and each subject's T1w/T2w image and hippocampus segmentation were warped to the population average (2.3 Image Processing). Fractional anisotropy (FA) and mean diffusivity (MD) maps were obtained for each subject, and warped to the population average (2.3 Image Processing). In the population specific common space, masking of T1w/T2w, MD and FA images (microstructural images) using a whole hippocampus segmentation results in 3 vectors of voxel-wise microstructural metrics for each subject, for both the left and right hippocampus (6 vectors in total). These vectors were used to build an input matrix for the NMF algorithm to perform a decomposition analysis. The NMF output subject weightings were used to describe group and individual level microstructural patterns, and output spatial components were used to visualize the spatial specificity of these patterns (2.4 Non-negative matrix factorization). Stability of output spatial components was assessed using an iterative procedure in which all subjects at study

are split into two groups, NMF is performed on microstructural data for each group, and the similarity between the output components is assessed (2.4.3 Stability Analysis). We also assessed stability of output spatial components when using only one microstructural metric at a time in comparison to three metrics (2.4.4 Unimodal Analysis). Finally, output subject weightings were related to a set of demographic and cognitive variables using a partial least squares analysis (2.5 Microstructure-Behaviour Relationships).

2.2. Data

We used data from the Human Connectome Project (HCP) Young Adult dataset (Van Essen et al., 2013), a publicly available dataset consisting of multimodal MRI data for a total of 1200 healthy young adults (age 22–35). Because this dataset contains twin and non-twin subjects, a subset of 333 unrelated subjects were selected for analysis in order to avoid any potential biases related to family structure. All MRI data were acquired on a Siemens 3T Skyra with a custom 100 mT/m gradient (Van Essen et al., 2013; Van Essen et al., 2012). We used T1-weighted (T1w) and T2-weighted (T2w) structural (0.7 mm^3 voxels) and diffusion (1.25 mm^3 voxels) weighted MRI data. Sequence parameters have been published elsewhere (Andersson et al., 2012; Glasser et al., 2013; Sotiropoulos et al., 2013; Uğurbil et al., 2013; Van Essen et al., 2012), and can be found in the Supplementary Materials.

T1w and T2w images used in this manuscript underwent preprocessing conducted by the HCP including: gradient distortion correction, co-registration of repeated runs using a 6-DOF rigid body transformation followed by averaging, ACPC alignment to MNI space, brain extraction, and readout distortion correction. The corrected T2w image was registered to the T1w image to allow for creation of the T1w/T2w ratio image, and both T1w and T2w images were then corrected for bias field inhomogeneities (Glasser et al., 2013; Glasser and Van Essen, 2011). In this work, we utilized the preprocessed T1w, T2w and T1w/T2w images provided through the HCP informatics portal (https://db.humanconnectome.org/). In subsequent steps, a combination of structural and diffusion MRI-based metrics was used to assess microstructure for each subject. Specifically, T1w/T2w, MD and FA images were used as complementary measures of tissue microstructure.

2.3. Image Processing

The goal of image preprocessing in this work was to obtain hippocampus segmentations for each subject, compute a population average to create a common space, and non-linearly warp structural (T1w/T2w images) and diffusion (MD, FA images) to the common space.

2.3.1. Automatic hippocampus segmentation

Hippocampus segmentations for each subject were obtained using the MAGeT Brain algorithm (Chakravarty et al., 2013; Pipitone et al., 2014). This approach uses a variation of standard multi atlas procedures to segment each image in a dataset. Five high resolution manually segmented atlases were used as input (Winterburn et al., 2013). In these atlases, cornus ammonis (CA) 1, CA2/CA3 (CA2CA3), CA4/dentate gyrus (CA4DG), stratum radiatum/stratum lacunosum/stratum molecular (SLRM), and subiculum are labelled as separate structures (Winterburn et al., 2013). Twenty-one images from the subject set were then selected as templates through which atlas-subject segmentations are bootstrapped. The non linear registration of each of the 5 atlases to each of the 21 templates results in a study specific set of 21 atlases. Then, non linear registration of each template to each subject creates 105 unique atlas-template-subject transformations through which atlas segmentations are warped. At the subject level, a majority vote was used to fuse the 105 candidates to create the final segmentation. Non-linear registration was performed using a minc-toolkit compatible version of the Automatic Normalization Tools registration (Avants et al., 2008) (https://github.com/vfonov/mincANTS). Each hippocampus segmentation was manually quality controlled by author SP, with assistance from RP. While the above workflow describes protocol for obtaining hippocampal subfield segmentations, subfields were subsequently fused together to create a whole hippocampus segmentation required for this work, as we have done in previous studies (Sankar et al., 2017; Voineskos et al., 2015).

2.3.2. Diffusion preprocessing

We downloaded preprocessed diffusion data from the HCP. The full HCP diffusion preprocessing pipeline is described elsewhere (Glasser et al., 2013). It includes EPI distortion correction using topup, eddy current and motion correction for each volume using eddy. Further diffusion preprocessing was performed with MRtrix (https://github.com/MRtrix3/mrtrix3) (Tournier, Calamante and Connelly, 2012) in order to obtain MD and FA maps for each subject. Briefly, this involved computing the tensor image using iteratively reweighted linear least squares (dwi2tensor) (Veraart et al., 2013) followed by estimation of MD and FA maps (tensor2metric) (Basser et al., 1994; Westin et al., 1997). Single shell ($b = 1000$) data were supplied to dwi2tensor to compute the tensor, in accordance with typical diffusion tensor approaches (Jones and Basser, 2004; Tournier, Mori and Leemans, 2011; Veraart et al., 2013).

2.3.3. Population average creation

To obtain voxel-wise correspondence, a population average was created for the 333 subjects included in the present study. First, each subject's T1w and T2w images were cropped using a bounding box with limits derived from the subject's hippocampal segmentation in order to emphasize registration accuracy in the area of interest for this study (Chakravarty et al., 2008). Then, the ANTs multivariate template construction tool (Avants et al., 2010) was used to construct the population average image, using each subject's cropped T1w and T2w image as input. Both T1w and T2w images were used to capitalize on the high quality multimodal data available in the HCP and improve registration through the use of complementary contrasts.

The resulting non linear transformations were used to warp each subject's T1w/T2w, MD and FA images to the population average using antsApplyTransforms, with the population average as the reference image and resampled with b-spline interpolation (this results in upsampling MD and FA images to match the 0.7 mm resolution of the population average). After resampling, T1w/T2w, MD and FA images were zero bounded to remove any potential artifacts of b-spline interpolation. To ensure abnormal T1w/T2w values did not remain, a filtering was also applied similar to that used in previous works (Glasser and Van Essen, 2011), but replacing geodesic distance with Euclidean distance as this work is in volumetric space as opposed to surface based. Briefly, the T1w/T2w value at a given voxel was compared to it's neighbourhood (includes 12 voxels in each of x,y,z directions), and any T1w/T2w value more than 2 standard deviations away from the neighbourhood mean was replaced with a gaussian weighted average of the neighbourhood (fwhm = 5 mm). Each subject's hippocampus segmentation was also warped to the population template using the antsApplyTransforms tool with GenericLabel resampling. In the template space, majority voting of all hippocampus segmentations that passed quality control was used to produce the hippocampus segmentation for the population template.

2.4. Non-negative matrix factorization

In this work we employ an orthogonal variant of NMF, orthogonal projective NMF (OPNMF) (Sotiras et al., 2015; Yang and Oja, 2010) in order to ensure output spatial components are non overlapping, and that each output component represents a distinct pattern. This aids interpretation and allows easy assignment of each voxel to a particular component for a purely additive parts based representation.

2.4.1. OPNMF background

OPNMF decomposes a given input matrix of dimensions m x n into a component matrix W (m x k), and a weight matrix H (k x n). The number

of components, k, is defined *a priori* by the user. The component and weight matrices are constructed such that their multiplication reconstructs the input data as best as possible (Fig. 1) by minimizing the reconstruction error between the original input and the reconstructed input ($W \times H$). As previously described (Sotiras et al., 2015; Varikuti et al., 2018), OPNMF estimates W and H by solving the minimization problem:

$$||X - WW^TX|| \text{ subject to } W^TW = I; W \geq 0 \quad (1)$$

Where $||||$ represents the squared Frobenius norm. Note that I represents the identity matrix, thus enforcing orthogonality among the columns of W. W is initialized using non-negative double singular value decomposition (Boutsidis and Gallopoulos, 2008). This choice of initialization encourages sparsity in the output components. These key features ensure sparse, non-overlapping output spatial components such that each voxel can be easily assigned to an output component using a winner take all strategy which eases the interpretability of the output spatial patterns. Following initialization, W is updated using a multiplicative update rule:

$$W^{'}_{ij} = W_{ij}\frac{(XX^TW)_{ij}}{(WW^TXX^TW)_{ij}} \quad (2)$$

Finally, the weight matrix H is calculated by projecting the input X onto W:

$$H = W^TX \quad (3)$$

The identified components can be interpreted as representing "parts" of the original input, giving the method the ability to identify underlying patterns of variance in multivariate data (Lee and Seung, 1999). The weight matrix then describes the loading, or dependence, of each sample on a given component in the reconstruction of the original input matrix.

2.4.2. OPNMF implementation

In this implementation, each column of the input matrix contained voxel-wise data for a given subject-metric combination. 329 out of 333 selected subjects were analyzed with OPNMF, due to 3 subjects missing cognitive data and 1 subject with abnormal DWI data. To begin, masked extraction, using the fused template hippocampus segmentation, results in a total of 6 vectors describing hippocampus microstructure for each subject (3 microstructural metrics for each of left and right hippocampus). Since microstructural metrics exist in scales of varying magnitude, a normalization was required. First, a z-scoring was performed in a within-metric, within-hemisphere fashion. Then, within each hemisphere, the resulting z-scored values were all shifted by the minimum z-score in order to align the histogram of each left/right hippocampus microstructural metric and ensure each metric is on the same scale (Supplementary Material - Constructing the input matrix).

Given three microstructural metrics (T1w/T2w, FA, MD) and analysis of 329 subjects, the input matrix contains $329 \times 3 = 987$ columns for a given hemisphere. Columnar stacking was organized by metric, such that the first 329 columns correspond to T1w/T2w data, the second 329 columns to MD data, followed by 329 columns of FA data. It follows that the number of rows corresponds to the number of voxels in the hippocampus. Thus, each column of the input matrix represents microstructural characteristics of a given subject. For unimodal analyses, the appropriate 329 columns were selected from the multimodal input matrix. For example, in OPNMF analyses of only MD, the input matrix consists of the second set of 329 columns from the multimodal input matrix.

OPNMF was conducted separately on each of the left and right input matrices, representing the left and right hippocampus. We used publicly available code available at https://github.com/asotiras/brainparts (Boutsidis and Gallopoulos, 2008; Halko et al., 2011; Sotiras et al., 2015; Yang and Oja, 2010) and Matlab R2016a. OPNMF was run with non-negative double singular value decomposition initialization, max iterations = 100000 and tolerance = 0.00001.

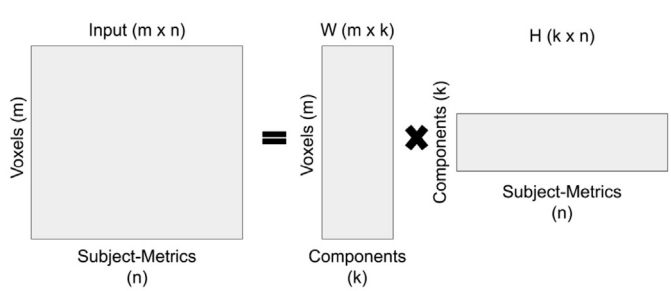

Fig. 1. A schematic representation of non-negative matrix factorization (NMF). NMF and it's variants decompose an input matrix into two matrices - a component matrix W and weight matrix H. NMF aims to minimize the reconstruction error between the original input and the reconstructed input ($W \times H$).

2.4.3. Stability analysis

To select the optimal number of components to analyze, we assess both accuracy and stability of a decomposition. Accuracy is measured by observing the gradient in reconstruction error, enabling quantification of the gain in accuracy provided by increasing the number of components from one granularity to the next (Durran, 2013; Fornberg, 1988; Quarteroni et al., 2007). To assess stability, we look at the similarity of output spatial components across varying splits of data. The 329 subjects at study are randomly split into two groups (n_a = 164, n_b = 165). OPNMF is performed on each split independently to produce two component matrices Wa and Wb (with size = # of voxels x k). For each of these outputs, we compute a similarity matrix c_W by computing the cosine similarity between each row of W (c_W has size = # of voxels x # of voxels). In other words, c_W is a matrix where each row contains the cosine similarity of component scores between a given voxel and all other voxels. Finally, we compute the correlation coefficient between corresponding rows of c_Wa and c_Wb to quantify if the OPNMF decomposition groups a given voxel with the same subset of voxels in each split of data. We take the mean correlation across all voxels to represent the stability of a given granularity. A correlation coefficient of 1 represents perfect stability, whereas −1 would represent instability. We repeat the above procedure for 10 random splits of data, for k = 2 to 10.

2.4.4. Unimodal analysis

In order to assess the benefits of using multiple microstructural metrics, we performed a series of unimodal analyses as well. For each of the three microstructural metrics used, we conducted the previously described stability analysis using only a single metric at a time (6 total analyses - 3 metrics x 2 hemispheres), for granularities from 2 to 10. OPNMF was performed as described in Section 2.4.2, but in this case the input matrix has dimensions # of voxels x # of subjects.

2.4.5. Interpreting OPNMF output

The OPNMF analysis has two outputs - component matrix W contains the component scores of each voxel; weight matrix H describes the weightings of each subject-metric combination onto each component. Together, these two outputs are used to interpret three main results: group level microstructural patterns of each identified component (e.g. T1w/T2w signal is higher compared to MD), individual/subject level microstructural variation (e.g. Subject 1 shows higher T1w/T2w compared to Subject 2), and the spatial location of each identified component (e.g. T1w/T2w signal is higher compared to MD in these voxels).

W and H are computed so as to optimize the similarity of the original input and the reconstructed input ($W \times H$). Thus, the pairing of a high voxel component score in W and high weighting in H results in a significant contribution to the value of the corresponding element of the original input matrix. In the context of this study, W_{ik} is the component

score of voxel i in component k. A high score suggests this voxel is a part of the identified variance pattern. H_{kj} describes the weight of the subject-metric j for component k. If this is high, this indicates that the given metric is present in voxel i, for subject j. For high W_{ik}, an observed general pattern of $H_{1:329,k} > H_{330:658,k}$ suggests that across the group, T1w/T2w signal is more pronounced in voxel i than MD (group level). Concurrently, we may also observe subject-wise, within-metric variance in H: if H_{1j} is higher than H_{2j}, this suggests that Subject 1 has higher T1w/T2w signal in voxel i than Subject 2 (individual level).

Given the orthogonality constraint employed, voxels can be assigned to a component using a simple winner take all strategy in which a voxel is assigned to a component based on the highest component score ($max(W_{i,:})$). Assignments are then mapped back to the population average in order to visualize the spatial location of each component. In a final step, the properties and patterns of the weight matrix were used to interpret the patterns in each spatial component as described above.

2.5. Microstructure-behaviour relationships

To capitalize on the ability of OPNMF to identify individual level variability in addition to bulk group level patterns, we related individual subject weightings to performance on cognitive tasks assessed by the HCP. We considered 13 cognitive tests that spanned 7 cognitive subdomains (Barch et al., 2013; Van Essen et al., 2013) which have been linked to hippocampal function - episodic memory (Dickerson and Eichenbaum, 2009; Terry et al., 2015), executive function (cognitive flexibility) (O'Shea et al., 2016; Papp et al., 2014), fluid intelligence (Reuben et al., 2011), processing speed (O'Shea et al., 2016; Papp et al., 2014), impulsivity (Lebreton et al., 2013; Peters and Büchel, 2010), spatial orientation (Burgess, Jeffery, & O'Keefe, 1999; O'Keefe and Dostrovsky, 1971), and verbal episodic memory (Ezzati et al., 2016; Fletcher et al., 1997; Nyberg et al., 1996). Specific instruments used to assess each domain can be found in the Supplementary Materials (Table S1) as well as in (Barch et al., 2013). Histograms displaying the range of scores and demographic data for the subjects at study can also be found in the supplementary (Fig. S2).

2.5.1. Partial least squares analysis

To investigate any relationships between individual subject OPNMF weightings and individual variability in cognitive performance, we used partial least squares analysis (PLS). PLS is a multivariate technique which seeks to find patterns of covariance between two sets of variables (Krishnan et al., 2011; McIntosh and Lobaugh, 2004; McIntosh and Mišić, 2013). Here, we employ a behavioural PLS in which the brain data is a 329×12 matrix containing output OPNMF weights for each subject from the 4 component solution, and the behavioural data corresponds to a 329×16 matrix containing age, sex, years of education and cognitive performance across 13 tests (as described above) for each subject. PLS analysis outputs latent variables (LV), each of which describe linear combinations of the brain and behavioural data which maximally covary. Thus, each LV describes a pattern of associated microstructural and behavioural characteristics. For each LV, PLS computes a singular value which is used to compute the proportion of total covariance accounted for by a given LV.

Statistical significance of each LV is assessed via permutation testing. The rows of the brain data matrix are permuted 10000 times, with each permuted matrix used to compute a null distribution of singular values under the assumption that the permutations remove any existing brain-behaviour correlations. From this, a non parametric P value can be computed for each LV in the original, non permuted data. A threshold of $P < 0.05$ was used, corresponding to 95% or greater chance that the singular value of the non permuted data exceeds that of a permuted singular value. Bootstrap resampling is used to assess the contribution of each brain variable to a given LV. Random sampling with replacement of the rows of X and Y is conducted to generate 10000 resampled sets of brain and behaviour data which are then used to generate a distribution of the singular vector weight of each brain variable in each LV. When analyzing the original brain and behaviour data, the ratio of the singular vector weight over the standard error of the weight from the bootstrap distribution (bootstrap ratio, BSR) is used to assess the contribution and reliability of a given brain variable. We used a BSR threshold of 2.58, analogous to a p-value of 0.01 (Krishnan et al., 2011; McIntosh and Lobaugh, 2004; Nordin et al., 2018; Persson et al., 2014; Zeighami et al., 2017).

3. Results

3.1. Data

The final sample size included 329 subjects from the Human Connectome Project (Mean Age: 28.44 years ± 3.70 years; F/M: 185/144; Handedness: 63.57 ± 45.97).

3.2. Image Processing

318 of 329 MAGeT Brain hippocampus segmentations passed quality control. Thus, 318 segmentations were majority voted to create the population template hippocampus segmentation used to extract microstructural metrics (a failed hippocampus segmentation did not exclude a subject from OPNMF microstructural analysis). Fig. 2 shows the T1w population average created using the ANTs multivariate template construction tool.

3.3. Stability analysis

The results of the stability analysis are shown in Fig. 3. Fig. 3A plots both the stability coefficient (red) and gradient of the reconstruction error (blue) for $k = 2$ to 10, for each of the left and right hippocampus. In both hemispheres stability is shown to have an inverse relationship with k. At $k \geq 4$, stability coefficients are above 0.8 in both hemispheres. In the left hippocampus, notable drop offs in stability are observed when moving from $k = 4$ to both $k = 5$ and $k = 6$, after which stability levels off. In the right hippocampus, a sharp drop is seen when moving from $k = 4$ to $k = 5$. These results suggest $k = 4$ as a suitable choice for observing complex yet stable spatial patterns.

The gradient of the reconstruction error shows a positive relationship with k, as more components allow the decomposition to recover an increasing number of patterns. In both hemispheres, a sharp decrease in the magnitude of the reconstruction error gradient is observed when moving from $k = 4$ to $k = 5$. Recalling that, for each k, the value plotted represents the change in reconstruction error when moving from k-1 to k, these results show that the gain in accuracy when moving from $k = 4$ to $k = 5$ is much less than when moving from $k = 3$ to $k = 4$. For $k > 5$, there is less change in the gradient from one component to the next, as each added component adds a smaller, more stable gain to the reconstruction error. These observations suggest that at $k = 4$, the most prominent patterns have been captured and any added complexity has a diminishing return on reconstruction accuracy. Together with the results of the stability analysis, these results show $k = 4$ as a suitable selection for extended analysis.

3.3.1. Unimodal stability analysis

Fig. 3B plots stability coefficients for granularities from $k = 2$ to $k = 10$ when analyzing each metric individually as well as when using all three microstructural metrics together (red line in Fig. 3A is the same as the red line in Fig. 3B). In both the left and right hippocampus, stability of the unimodal spatial components was found to be lower than the multimodal components. In the multimodal analysis, stability coefficient was above 0.8 for $k = 2$–4, but only $k = 2$ in the right hippocampus reaches this (arbitrary) threshold. It follows that none of the unimodal analyses offered spatial components with stability matching that of the

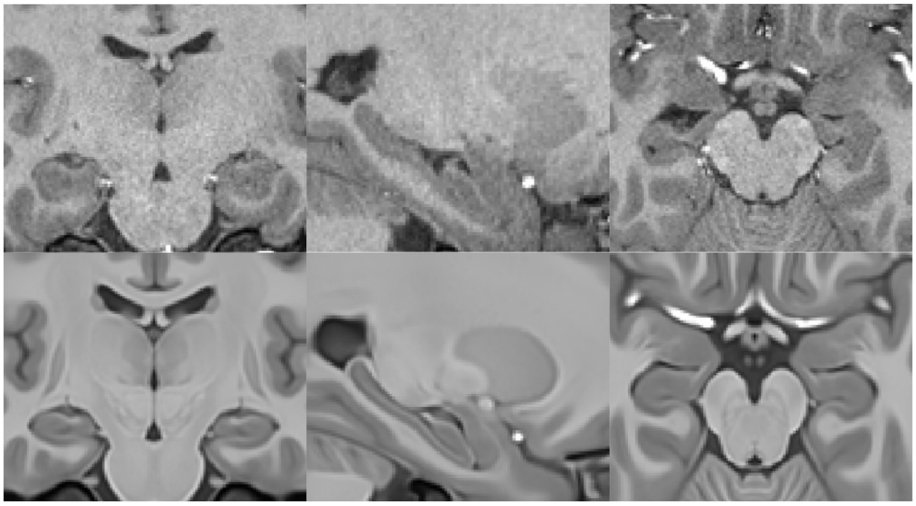

Fig. 2. Coronal, sagittal, and axial views of a single T1w image (top row) and T1w population average (bottom row). Both T1w and T2w images were used to drive registration between all subjects, in order to capitalize on the high quality multimodal data available.

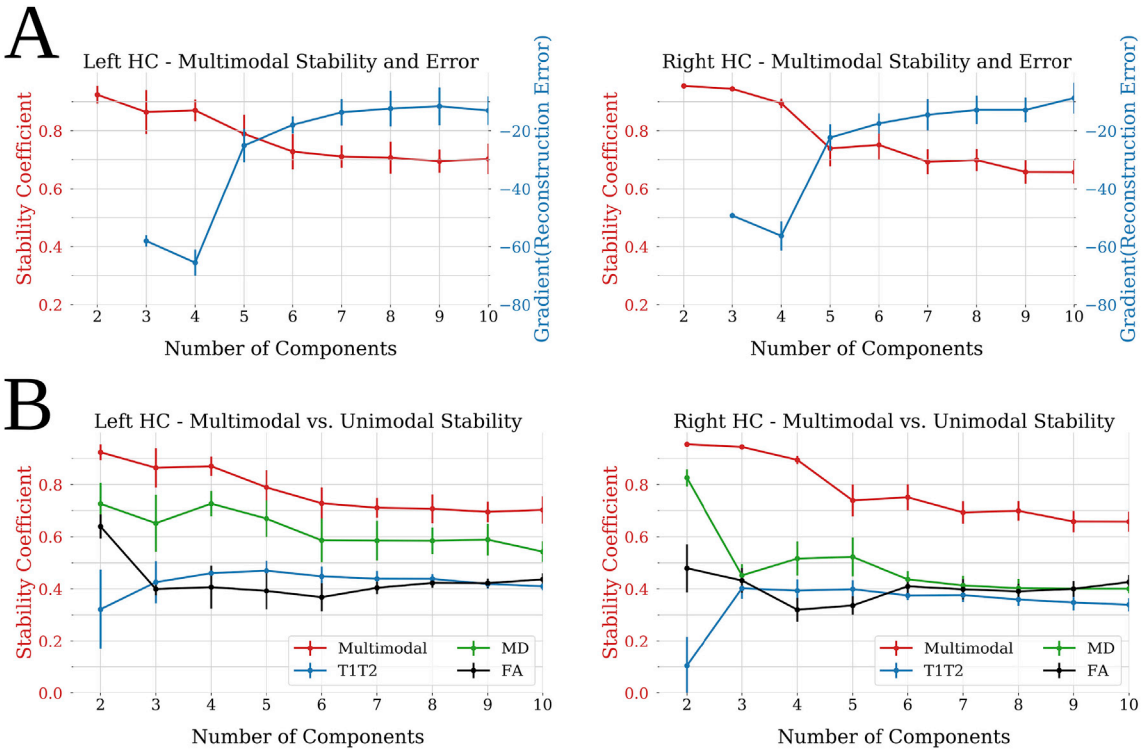

Fig. 3. Stability coefficient and gradient of the reconstruction error for granularities from 2 to 10 for the multimodal analysis (3A) and a comparison of stability coefficients of granularities from 2 to 10 for multimodal ("Multimodal"/red line) vs unimodal ("T1T2", "MD", "FA"/blue, green, black lines) analyses (3B). 3A: For both the left and right hippocampus, $k = 4$ was chosen a suitable balance of stability and reconstruction accuracy as stability (red line) drops off at $k \geq 5$, and the change in reconstruction error (blue line) from $k = 4$ to $k = 5$ is much less than from $k = 3$ to $k = 4$. 3B: For both the left and right hippocampus, unimodal decompositions ("T1T2", "MD", "FA"/blue, green, black lines) had notably lower stability than multimodal decompositions ("Multimodal"/red line).

$k = 4$ solution selected from the multimodal analysis. These results show that the use of multiple microstructural metrics enables finer scale, more stable parcellations to be created. Due to the notably lower stability, we do not present components or PLS analysis for any of the unimodal approaches.

3.4. Neuroanatomical description of 4 component solution

Fig. 4 displays the 4 component solution of both the left and right hippocampus, including both a 3-dimensional volumetric rendering (Fig. 4A) and coronal views of representative slices (Fig. 4B). Fig. 4C displays the subject weight matrix, used to describe both the group and individual level microstructural patterns associated with each component. Each row has been z-scored in order to better compare the prominence of each metric within each component (raw subject weight matrices can be found in the Supplementary Materials Fig. S3). For simplicity, only the weight matrix for the left hippocampus is shown as the right weight matrix draws similar conclusions (Supplementary Materials Fig. S3).

We characterize each component by describing it's microstructural

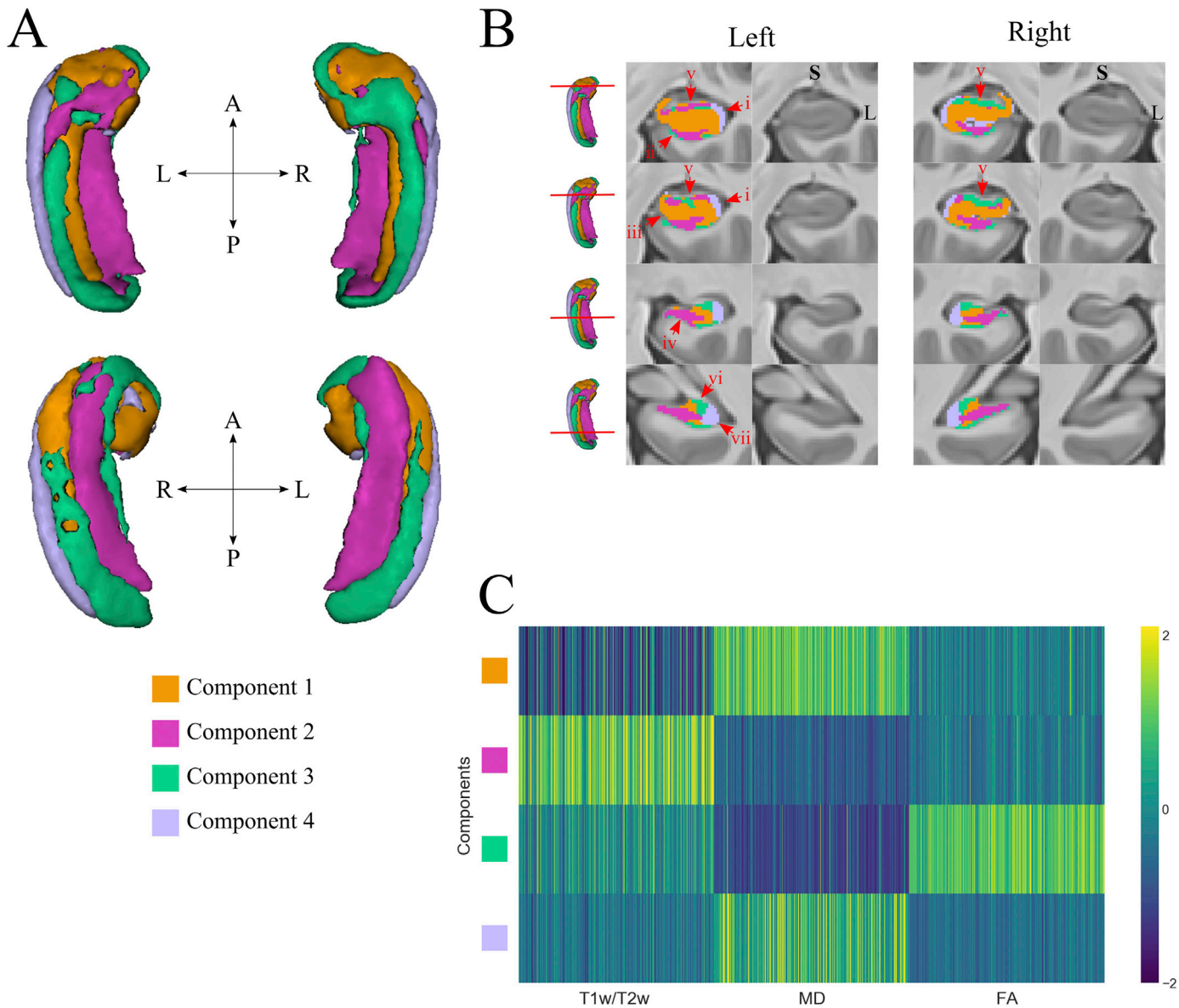

Fig. 4. The 4 component solution for both the left and right hippocampus, including 3-dimensional volumetric rendering (4A), coronal views of representative slices (4B), and z-scored weight matrix for the left hippocampus (4C). In 4A, the top row corresponds to superior views of the left and right hippocampus and the bottom row shows inferior views. In 4B, coronal slices are shown for the left and right hippocampus along with corresponding unlabelled anatomical slice. The hippocampal figure along with horizontal red line denotes where the slice resides along the anterior-posterior hippocampus. Red lettering i through vii describes specific anatomical features of each component. i) component 1 spans the majority of the lateral-medial extent in the hippocampal head, except for the lateral band occupied by component 4; ii, iii) component 1 spans only the mid portions of the superior-inferior axis of the hippocampal head; iv) component 2 resembles the subiculum along with medial aspects of the SLRM and CA1 subfields; v) superior band of component 2 is more prominent in the left hippocampus than in the right; vi) in the posterior hippocampus, component 3 occupies a wedge shaped cluster of voxels; vii) component 4 thickens from a thin band in the anterior hippocampus to a wedge shaped cluster of voxels along the lateral edge. 4C shows the normalized weight matrix which can be used to visualize comparative microstructural features of each component. Coloured boxes specify the corresponding component in 4A and 4B of each row, and text along the x axis denotes ordering of microstructural features. Volumetric rendering created using Mango (http://ric.uthscsa.edu/mango/index.html).

features as well as its anatomical location along each of the three axes (anterior-posterior, lateral-medial, superior-inferior). While the resolution of the data preclude us from making conclusions regarding subfields, where appropriate we use hippocampal subfields to help describe location in a purely descriptive, qualitative manner. The identified microstructural patterns are bilateral, though the ordering varies slightly between hemispheres. Left component 2 corresponds to right component 3 and vice versa. For simplicity, we adopt the ordering from the left hippocampus throughout the rest of the paper and discussion. Note that this adjustment was made prior to creation of Fig. 4, such that do not need to consider this when viewing Fig. 4.

Component 1 is characterized by high MD, low T1w/T2w, and low FA (Fig. 4C, row 1). It spans the full length of the anterior-posterior axis, but is more prominent in the anterior half of the hippocampus (Fig. 4A and B, orange). In the hippocampal head, component 1 spans the majority of the lateral-medial extent of the hippocampus (with the exception of the thin lateral band occupied by component 4, Fig. 4B, i), but along the superior-inferior axis it is present only in the mid portions (resembling the CA4DG subfield along this axis, Fig. 4B, ii, iii).

Component 2 is characterized by low MD, high T1w/T2w and low FA (Fig. 4C, row 2). This component spans the full anterior-posterior extent, but is largely confined to the superior and inferior regions of the

hippocampus (Fig. 4A and B, pink). Inferiorly, component 2 often resembles the subiculum along with medial aspects of the SLRM and CA1 subfields (Fig. 4B, iv). In the hippocampal head, component 2 is also found in a thin horizontal band of voxels in the superior hippocampus. This superior band of component 2 is more prominent in the left hippocampus than in the right (Fig. 4B, v).

Component 3 is characterized by low MD, marginal T1w/T2w), and high FA (Fig. 4C, row 3). Similar to component 2, it spans the full anterior-posterior extent but only in superior and inferior regions (Fig. 4A and B, green). Inferiorly, it typically occupies a thin band of voxels sitting inferior and lateral to component 2 (localized to the subiculum and inferior CA1 subfields). In the posterior portion of the hippocampus, component 3 occupies a wedge shaped cluster of voxels found separating the superior portions of components 1 and 4 (Fig. 4B, vi). In anterior portions of the hippocampus, component 3 can be described as a thin horizontal band sitting superior to component 1 and is more prominent in the right hippocampus than the left (Fig. 4B, v).

Component 4 has a similar microstructural profile to component 1, with high MD, low T1w/T2w and low FA (Fig. 4C, row 4). However, while MD is high in comparison to T1w/T2w and FA in this component, we note that it's overall magnitude is lower than that of component 1 (Supplementary Material). It is found exclusively in the lateral hippocampus, throughout most of the anterior-posterior extent (Fig. 4A and B, light purple). In the anterior portion of the hippocampus, component 4 is seen as a thin vertical band located along the lateral edge of the hippocampus (Fig. 4B, i). In the posterior portion of the hippocampus however, it thickens from a thin band to a wedge shaped cluster of voxels while maintaining its location along the lateral edge (Fig. 4B, vii).

3.5. Microstructure-behaviour relationships

To investigate any relationships between individual subject OPNMF weightings and individual variability in cognitive performance, we performed a behavioural PLS analysis where the brain variables correspond to the output OPNMF weightings from the 4 component decomposition, and behaviour variables corresponded to a set of demographic and hippocampus specific cognitive variables (Section 2.5). PLS analysis revealed four statistically significant latent variables (LV), two for each of the left ($ps < 0.001$) and right ($ps < 0.05$) hippocampus. Each LV displayed a unique pattern of microstructural and cognitive correlation (Fig. 5).

3.5.1. Left LV1

Left LV1 accounted for 49% of variance explained (Fig. 6). The cognitive and demographic variables contributing to left LV1 included older age ($R = 0.128$, 95% $CI = [0.022,0.233]$), female sex ($R = 0.347$, 95% $CI = [0.27,0.423]$), increased episodic memory performance ($R = 0.211$, 95% $CI = [0.133,0.297]$), increased delay discounting performance ($R = 0.107$, 95% $CI = [0.017,0.203]$), and slower reaction time in spatial orientation tests ($R = 0.121$, 95% $CI = [0.038,0.205]$) (Fig. 5A). The correlating microstructural features included decreased MD in components 1–3 (Fig. 5B). While the females in the sample at study do have slightly increased age in comparison to males (mean female age $= 29.01 \pm 3.62$, mean male age $= 27.71 \pm 3.67$) the notably larger contribution of sex to left LV1 does suggest a unique contribution of sex to this microstructure-behaviour pattern.

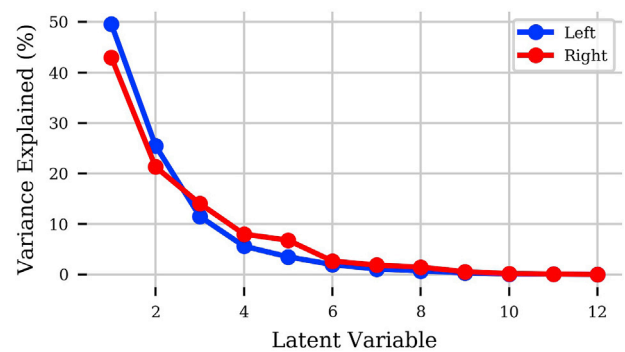

Fig. 6. The variance explained by each latent variable for both the left and right hippocampus. Only the first two latent variables were considered significant via permutation testing for both the left and right hippocampus (% variance explained < 20% for all non significant latent variables).

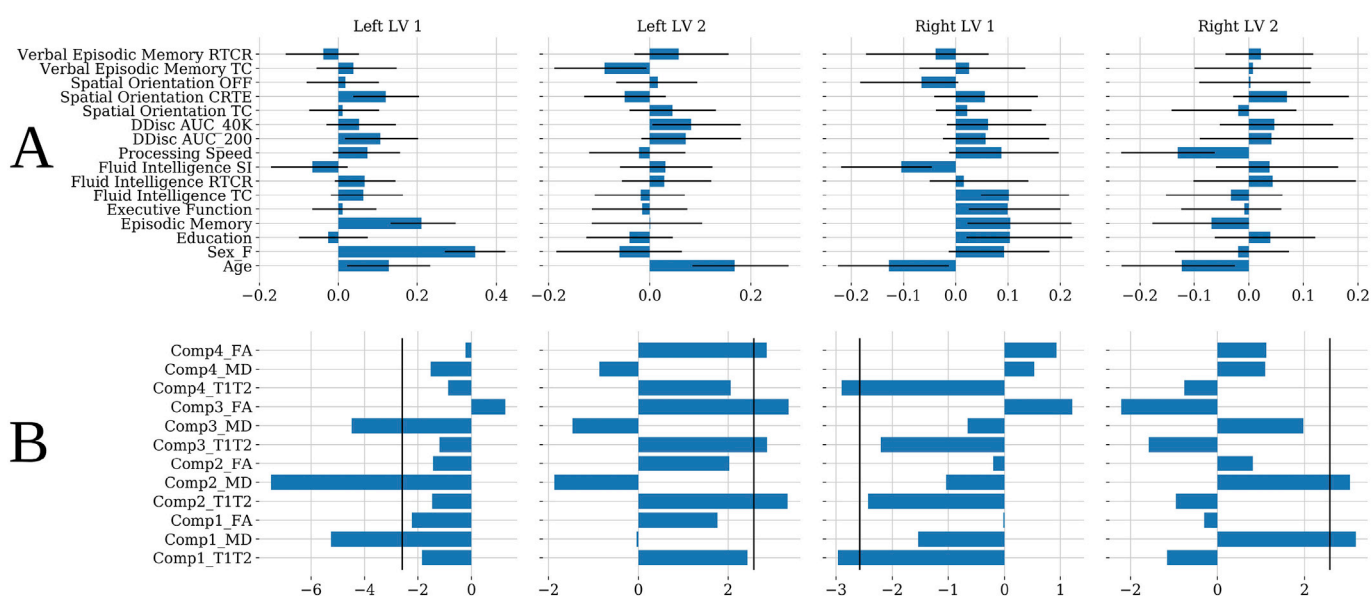

Fig. 5. The behavioural (5A, top row) and microstructural (5B, bottom row) patterns of each latent variable (ordered by column from left to right: Left LV1, Left LV2, Right LV1, Right LV2). In 5A, the y-axis the demographic/behavioural measure while the x-axis denotes correlation within a given LV. In 5B, the y-axis denotes the component/microstructure metric while the x-axis denotes the bootstrap ratio. The black lines in 5B correspond to the BSR threshold of 2.58. Abbreviations: TC: Total correct responses; SI: Skipped items; RTCR: Median reaction time for correct responses; CRTE: Median reaction time divided by expected number of clicks for correct trials; OFF: Total positions off for all trials.

3.5.2. Left LV2

Left LV2 accounted for 25% of variance explained (Fig. 6). The cognitive and demographic variables contributing to left LV2 included older age (R = 0.167, 95% CI = [0.084,0.274]), increased delay discounting performance (R = 0.082, 95% CI = [0.005,0.180]), and decreased verbal episodic memory performance (R = −0.089, 95% CI = [-0.188,-0.006]) (Fig. 5A). The correlating microstructural features included increased T1w/T2w in components 2 and 3, and increased FA in components 3 and 4 (Fig. 5B).

3.5.3. Right LV1

Right LV1 accounted for 43% of variance explained (Fig. 6). The cognitive and demographic variables contributing to right LV1 included young age (R = −0.128, 95% CI = [-0.225,-0.013]), increased education (R = 0.104, 95% CI = [0.020,0.223]), and increased performance on tests of episodic memory (R = 0.105, 95% CI = [0.022,0.222]), executive function (R = 0.099, 95% CI = [0.025,0.200]), and fluid intelligence in terms of both correct items (R = 0.102, 95% CI = [0.048,0.217]) and fewer items skipped (R = −0.104, 95% CI = [-0.219,-0.046]) (Fig. 5A). The correlating microstructural features included decreased T1w/T2w in components 1 and 4 (Fig. 5B).

3.5.4. Right LV2

Right LV2 accounted for 21% of variance explained (Fig. 6). The cognitive and demographic variables contributing to right LV2 included younger age (R = −0.124, 95% CI = [-0.234,-0.026]) and decreased processing speed (R = −0.131, 95% CI = [-0.234,-0.062]) (Fig. 5A). The correlating microstructural features included increased MD in components 1 and 2 (Fig. 5B).

4. Discussion

In this work, we used OPNMF to study patterns of hippocampus microstructure, as assessed by structural and diffusion MRI. At the group level, we identified k = 4 as a suitable choice for decomposing the hippocampus into microstructural parts, based on measures of stability and accuracy. We also compared the stability of a multimodal decomposition to that of a unimodal analysis to show that the use of three microstructure metrics increases OPNMF stability at a range of granularities, better allowing the algorithm to define boundaries between regions of varying microstructure. At the individual level, we related OPNMF weights to demographic and cognitive measures to identifying microstructure-behaviour relationships.

4.1. Group level microstructure

Component 1 described increased MD in a large portion of the hippocampal head, mostly corresponding with voxels in the CA4DG subfield. Recent work conducted using polarized light imaging described the CA4 region as hypointense, corresponding to a lack of myelin and/or less densely packed cell bodies (Zeineh et al., 2017). Furthermore, the authors used an in vitro receptor autoradiography analysis to visualize kainate receptor density and localize the unmyelinated mossy fibers as projecting from the DG, through the CA4 and to the CA3 region (Zeineh et al., 2017). Component 4 described similar microstructural characteristics as component 1 and included the lateral most aspects of the hippocampus, mostly spanning portions of the CA2CA3 and lateral CA1. It described increased MD in comparison to T1w/T2w and FA, albeit with less magnitude overall in comparison to component 1. Thus, we posit that this component is an extension of component 1 and may be capturing portions of the unmyelinated mossy fibers as well as the pyramidal layers of CA1 and CA2CA3.

Component 2 describes increased T1w/T2w in voxels overlapping with the subiculum and medial portions of the SLRM, potentially indicating increased myelination in these regions (Glasser and Van Essen, 2011). This may be representing the presence of the perforant pathway, the major hippocampal fiber bundle, known to travel from the entorhinal cortex through the subiculum via the angular bundle (Andersen et al., 2007; Duvernoy and Bourgouin, 1998). Zeineh et al. described the sigmoidal fibers of the angular bundle travelling through the subiculum (Zeineh et al., 2017). While the presence of these fibers would also suggest increased FA due to a preferred fiber orientation, component 2 shows low FA. We believe the presence of crossing fibers and the resolution of the data at study results in component 2 displaying characteristics of increased myelination but being unable to capture any increases in FA.

Other superior portions of components 2 as well of all of component 3 showed increased T1w/T2w and FA in the 'outer rim' of the hippocampus, corresponding to deepest parts of the CA1 and CA2/CA3 subfields. With reference to Zeineh et al., these findings correspond to the stratum oriens region of these subfields, which, in CA1, houses fibers from the alvear path and in CA3 contains the endfolial pathway (Zeineh et al., 2017). We also note that, at the resolution of diffusion MRI, adjacent structures including the alveus and fimbria which display white matter characteristics are likely playing a role through partial volume effects.

4.2. Individual microstructural variability

In addition to group level spatial patterns, we also investigated microstructure - behaviour relationships at the individual level. While group level analysis may provide insight to overall, normative patterns, analyses of individual variability move towards classifying or predicting outcomes for a given individual, while accounting for their unique characteristics. This difference is analogous to a group difference vs. classification distinction (Arbabshirani et al., 2017), and is perhaps more clear in the context of disease. Description of the pathological differences between health and disease, despite being a necessary precursor, may be less impactful than prediction of health vs. disease on an individual basis.

Our PLS analysis identified two significant LVs in each of the left and right hippocampus. Left LV1 and right LV2 both describe a pattern where MD was inversely correlated with age and some measure of cognitive performance (episodic memory and spatial orientation in the left, processing speed in the right). MD throughout most of left hippocampus was inversely related with age, female sex, episodic memory performance and reaction time in a spatial orientation task. Similarly, MD throughout much of the right hippocampus was inversely related with age and processing speed. The inverse relationship between MD and age may correspond to previously described developmental effects where MD increases with age. In particular, results from Lebel et al. showed the same age related trend across the early adulthood age range in deep grey matter structures (Lebel et al., 2008). In terms of behaviour, decreased performance of females in spatial orientation tasks (Gur et al., 2012; van der Linden et al., 2017) and increased performance in verbal episodic memory (Asperholm et al., 2019; van der Linden et al., 2017) have both been previously established.

Left LV2 describes a largely age related pattern in which older participants show increased T1w/T2w in the subicular and superior CA1 and superior CA2/CA3 regions, as well as increased FA in the subicular and lateral portions of the hippocampus. Behaviourally, this LV also included increased performance on delay discounting tasks and decreased verbal episodic memory performance. Previous works have identified non linear relationships between FA and age in white (Kochunov et al., 2012) and grey matter (Lebel et al., 2008). In particular, Lebel et al. identify these relationships in deep grey matter structures as well as cerebral white matter regions (Lebel et al., 2008). In work by Nazeri et al., orientation dispersion in the hippocampus was found to decrease slightly between the ages of 20 and 40, which would correlate with a similar increase in FA as shown here (Nazeri et al., 2015). Increases in cortical T1w/T2w within the age range at study have also been reported, with Grydeland et al. reporting an increase in T1w/T2w until the late 30s followed by a plateau and later decline, and Shafee et al. reporting a linear relationship between T1w/T2w and age (Grydeland et al., 2013; Shafee et al., 2015). In

this context, this LV potentially suggests an extension of maturational patterns previously described in the cortex and other subcortical regions to the hippocampus.

Finally, right LV1 contains widespread behavioural effects along with a maturational, age-related T1w/T2w pattern. Behaviourally, this LV describes a link between increased performance on a range of cognitive areas, including episodic memory, executive function and fluid intelligence, with increased years of education and younger age. That MRI derived measurements of the hippocampus relate to each of these behavioural measures is not surprising, as properties of the hippocampus have been related to each of episodic memory (Dickerson and Eichenbaum, 2009; Terry et al., 2015; Tulving and Markowitsch, 1998), executive function (O'Shea et al., 2016; Papp et al., 2014), and fluid intelligence (Reuben et al., 2011). Similarly, higher educational attainment has been linked to better performance on these measures as well (as described here) (Bilker et al., 2012; de Wit et al., 2007; Gur et al., 2010; Kaufman et al., 2009; Reimers et al., 2009). As previously discussed, the directionality of the age-T1wT2w relationship is in accordance with previous work (Grydeland et al., 2013; Shafee et al., 2015), suggesting that this LV links previously described demographic relationships with a hippocampal microstructural determinant. Interestingly this LV involves MD features localized to a large portion of the right hippocampus but tends to exclude subicular and CA1 regions.

The aim of this approach is to provide a behavioural characterization of the identified microstructural components. Interpretation of identified brain-behaviour relationships requires careful consideration. Kharabian Masouleh et al. showed that using mass univariate testing to relate brain structure to behaviour in healthy adults revealed few associations, and that the few identified relationships had low replicability (Kharabian Masouleh, Eickhoff, Hoffstaedter, Genon, & Alzheimer's Disease Neuroimaging Initiative, 2019). Conversely, relationships between age and behaviour were much more consistent (Kharabian Masouleh et al., 2019).

We attempt to combat these issues by using a combination of OPNMF and PLS. In comparison to univariate testing at every voxel, OPNMF identifies spatial components in which variance occurs, thus helping to narrow the search space from all voxels to a potentially more relevant set of voxels (see Section 4.3 for more). PLS is a multivariate approach which considers relationships across multiple variables as opposed to univariate testing (McIntosh and Mišić, 2013). PLS assesses significance of the identified latent variables through permutation testing, enabling an assessment of a latent variable's effect size against a null distribution. By identifying spatial regions of variance and assessing multiple behavioural/demographic variables simultaneously, we hope to account for some of the difficulties involved with interpreting univariate brain-behaviour relationships in healthy adults. Nonetheless, we caution that these results remain exploratory and requires further replication.

While the directionality of our results is in the expected direction, we also observed laterality effects - with the left hippocampus being related to delay discounting, verbal episodic memory and spatial orientation, the right hippocampus being related to executive function, processing speed and fluid intelligence, and the bilateral hippocampi being related to age and episodic memory. This is in accordance with some, but not all, previous works on the lateralization of hippocampal function. As found here, verbal episodic memory (Ezzati et al., 2016; Fletcher et al., 1997; Nyberg et al., 1996) has been predominantly associated with the left hippocampus. Episodic memory has been predominantly linked to the left hippocampus (Burgess, Maguire, & O'Keefe, 2002; Ezzati et al., 2016), but here was found to be related to the bilateral hippocampus. Performance in spatial tasks has been mainly linked to the right hippocampus (Burgess et al., 2002; Ezzati et al., 2016; Gur et al., 2000, 1982) but here was linked only to left hippocampus microstructure. Zhu et al. found correlations between bilateral hippocampi and fluid intelligence, although relationships with right hippocampus were stronger than left (Zhu et al., 2017). The role of the hippocampus in delay discounting tasks is typically discussed bilaterally (Lebreton et al., 2013; Peters and Büchel, 2010), but here was only implicated in the left hippocampus. Overall, it is unclear why some of our brain-behaviour relationships are lateralized as described above. We note the dataset at study is a young healthy population with minimal expected variation in cognitive performance (Kharabian Masouleh et al., 2019) and the observed correlational relationships are subtle in magnitude which may hinder our ability to observe specific laterality properties but still allow us to describe more gross microstructural-behavioural relationships. Overall, we feel that interpretations on laterality specifically here are inconclusive.

4.3. Identifying regions of variability

While less common than other techniques, this is not the first instance of NMF or its variants used in a neuroimaging context. Thompson et al. utilized NMF to assess patterns of genetic expression in the mouse hippocampus, parcellating the hippocampus into regions showing similar patterns of expression (Thompson et al., 2008). More recently, Sotiras et al. applied OPNMF to analyze FA in a mouse dataset, and separately used OPNMF to analyze grey matter data in a healthy aging cohort (Sotiras et al., 2015). In both cases they found that individual loading weights linked to age related variance, analogous here to our relation of subject weightings to cognitive performance. Importantly, this work also analyzed OPNMF in comparison to more commonly used decomposition techniques (Principal Component Analysis and Independent Component Analysis) to explicitly demonstrate the increased interpretation due to the non-negative restriction and resulting additive, parts based representation. On the other end of the developmental spectrum, Nassar et al. examined structural covariance patterns of grey matter in a young human dataset (some of which were born preterm). This approach identified biologically interpretable spatial clusters which shared covariance, and which resembled notable networks such as the visual and somatosensory networks (Nassar et al., 2018). Furthermore, the volume of certain output components was found to relate to an individual's gestational age (Nassar et al., 2018).

The works discussed above both contributed a similar analytical contribution which our work supports - the ability of OPNMF to identify regions in which relevant variation is occurring. This is especially helpful in a region such as the hippocampus, which has complex neuroanatomical structure and defining the subfields has become the topic of an international consortium tasked to reconcile existing differences in anatomical definitions and establish a standardized protocol for manual segmentation (Wisse et al., 2017). Indeed, the spatial components which were found to contain microstructural variation relevant to cognitive performance overlapped only partially with some subfields.

4.3.1. Data driven hippocampal clustering

Within recent years a number of studies have employed data driven clustering approaches to study the structural and functional architecture of the hippocampus. Each of these studies takes advantage of recent advances in data availability and quality, and a variety of algorithms and input data types have been applied in the specific case of the hippocampus (we focus here on hippocampal clustering for scope). K means clustering has been a popular choice, having been applied to hippocampal features derived from functional (Chase et al., 2015; Plachti et al., 2019; Robinson et al., 2016), structural (Plachti et al., 2019), and diffusion (Adnan et al., 2016) MRI. Spectral clustering has also been employed to cluster patterns of grey matter covariance (Ge et al., 2019). Other matrix decomposition approaches (ICA) have also been applied, more typically when analyzing functional MRI data (Beissner et al., 2018; Blessing et al., 2016; Zhao et al., 2019) but in some cases structural data as well (Ge et al., 2019).

For group level parcellations one method may not have distinct advantages over another. In fact, achieving widely varying results across methods may be driven by artifacts. Instead, we suggest each study consider their specific goals. The simplicity of k means may be preferential for purely group level parcellation. However if the goal is also to

analyze individual variability, the subject weightings from a decomposition would confer a notable utility as in the current work. Furthermore, in the case of functional analyses techniques such as ICA have been adapted to extend to analysis at the subject level (eg. using dual regression (Beissner et al., 2018; Blessing et al., 2016; Zhao et al., 2019). As described by Eickhoff et al., decomposition techniques offer flexibility to model data with varying distributions in comparison to the k means aim of deriving spherical clusters. Conversely, the hard cluster assignment of k means may be preferential to the continuous nature and potential overlap of output spatial components from a factorization approach (Eickhoff et al., 2018). In this approach, we aimed to capitalize on the orthogonal nature of OPNMF to easily assign voxels to distinct components using a winner take all approach while maintaining the flexibility of factorization approaches to generate a purely additive parts based representation of the hippocampus. For reference, nifti files of our microstructural parcellation has been made available at: https://github.com/raihaan/hc-nmf-micro.

4.4. OPNMF stability

Like other decomposition and clustering techniques, use of NMF and it's variants requires the user to select the granularity of choice for further analysis (Nassar et al., 2018; Sotiras et al., 2015, 2017; Varikuti et al., 2018). Our stability assessment approach splits the subjects at study, performs OPNMF on each subset, then assesses the spatial similarity of the outputs. This approach is based on previous cluster stability approaches (Ben-Hur et al., 2002) also used in current applications of OPNMF (Nassar et al., 2018; Sotiras et al., 2017). While assessing the same conceptual question, our approach compares vectors of component scores between voxels as opposed to comparing a hard cluster assignment. Thus, it can be seen as a continuous analog to the existing approaches which may have extended utility to NMF applications without strong orthogonality or sparsity constraints. We also employ multiple iterations, assessing stability between 10 different splits of data for each granularity. This iterative approach allows us to look at the variability of stability at a given granularity when making a selection, which may be highly relevant to datasets with large variability in demographics or diagnosis.

4.4.1. Stability vs. accuracy

Similar to related works, as granularity increases we observe a decrease in stability and an opposing increase in reconstruction error. In an analysis of adults age 49–85, Sotiras et al. applied OPNMF to voxel wise grey matter volume estimates and found that reproducibility of the spatial patterns was highest for lower number of components (<5), while age prediction accuracy using a support vector machine regression model with decomposition weights as input stabilized around 20 components (Sotiras et al., 2015). Varikuti et al. performed an age prediction using decomposition weights derived from an OPNMF decomposition of voxel wise grey matter volume estimates obtained from data across the lifespan. Analyzing a high range of granularity (50–690), they found their prediction accuracy stabilized only at $k = 300$, and spatial similarity of components between two datasets used peaked around $k = 150$ with a gradual decrease as complexity increased (Varikuti et al., 2018). Sotiras et al. used OPNMF to analyze cortical thickness data of a large sample of individuals aged 8–20 years. Reproducibility generally decreased as granularity increased, but showed peaks at $k = 2$, 7, and 18 (though reproducibility at $k = 2$ was much larger than that at $k = 7$ or 18), and the 18 component solution was selected for further analysis (Sotiras et al., 2017). Nassar et al., used OPNMF to analyze voxel wise grey matter volume estimates of individuals aged 8–22 at granularities from 2 to 30, finding that reconstruction error stabilized at 26 and reproducibility was high and stable for granularities from 6 to 30 (Nassar et al., 2018). Taken together, these studies, as well as ours, confirm the expectation that an increase in complexity comes with a trade off of accuracy vs. stability/reproducibility. Interestingly, in some cases the most stable solutions are at a lower granularity than that which gives best prediction accuracy (Sotiras et al., 2015; Varikuti et al., 2018). Similarly, as shown in our work, stability and reconstruction accuracy often have opposing trajectories with stability decreasing and reconstruction accuracy increasing with complexity. This important distinction highlights that while group level parcellations may describe general overall patterns, there still exists significant individual variation of the same patterns when considering an individual. We believe the framework proposed here, wherein we use OPNMF to assess individual variability within a group level description, may be a useful intermediary between group and individual level analysis. Thus, future work should always consider accuracy, stability, as well as their own specific goals in selecting a granularity for extensive analysis.

4.4.2. Multimodal vs unimodal

Using the stability approach described above, we found that the stability of unimodal OPNMF decompositions was notably lower than that of a multimodal decomposition. This validates a logical assertion that by providing more input information, OPNMF is better able to define fine scale spatial borders in a stable fashion. Based on this, we encourage future analyses employing OPNMF or other methods to utilize multiple metrics where possible in order to delineate more specific regions. This is especially relevant with the increasing prevalence of large scale multimodal datasets such as the Human Connectome Project (Van Essen et al., 2013), the Adolescent Brain Cognitive Development (ABCD) study (Casey et al., 2018; Jernigan, Brown, & ABCD Consortium Coordinators, 2018), and the UK Biobank (Alfaro-Almagro et al., 2018; Miller et al., 2016).

4.5. Limitations

The main limitation of this work lies in the confounds associated with structural and diffusion MRI as used in this study. Structural and diffusion MRI, even at the resolutions offered by the HCP, contain a mixture of numerous tissue types and associated structures in each voxel, resulting in each metric having uncertain physiological origin. Each of the four MR signals (T1w, T2w, MD, FA) utilized in this work can be described as 'sensitive but not specific'. Numerous biological phenomena, from myelination to axon degradation to changes in axonal orientation, may result in alterations in each of these signals (Jones et al., 2013; Tardif et al., 2016; Zatorre et al., 2012). Thus, although our use of multiple metrics may aid interpretation in comparison to a single metric analysis, at best we may still only hypothesize about the potential underlying cellular changes. Furthermore, at the resolutions used, partial voluming effects are a limitation of this approach. In particular, the hippocampus is bordered by white matter structures such as the alveus which have sharply different diffusion characteristics compared to the hippocampus. Given the adjacency of these structures to the region of interest at study, it can be expected that T1w/T2w, MD, and FA values of voxels in the deepest portions of the hippocampus are all impacted by partial voluming to some degree.

In this work, we employed the ratio of T1w and T2w signal (T1w/T2w) with the aim of using this metric as a correlate of myelin. This was based on previous studies that demonstrated correspondence between neocortical patterns of T1w/T2w and myelin (Glasser et al., 2016; Glasser and Van Essen, 2011). However, we acknowledge the more recent works suggesting T1w/T2w to be a less than optimal index of subcortical myelin (Arshad et al., 2017; Uddin, Figley, Marrie, Figley, & CCOMS Study Group, 2018). While the hippocampus is not a subcortical region, these recent works raise the possibility that correspondence between T1w/T2w and myelin is less than optimal in other non neocortical regions as well. Nonetheless, significant relationships between age and subcortical T1w/T2w have been reported (Tullo et al., 2019). Future use of quantitative MRI techniques, such as magnetization transfer or myelin water imaging to measure myelin instead of T1w/T2w, would help address this limitation (Tardif et al., 2016). We analyzed a population of

healthy young adults with a limited age range. While it is worth noting that OPNMF was able to capture the subtle variations of hippocampal microstructure (in relation to age related decline for example), a more impactful analysis would include data from a full age range and potentially identify critical points of change through the course of healthy aging. The use of longitudinal data in place of cross sectional data would enable more accurate mapping of any causal or sequential relationships between the brain and behaviour.

5. Conclusion

We used non-negative matrix factorization to analyze hippocampal microstructure, measured using multimodal data, in a young healthy population. Application of this technique identified spatial components of microstructural variance within the hippocampus, with 4 components being selected as a suitable balance between stability and accuracy. Importantly, spatial components derived from multimodal data were shown to be more stable across subsets of participants than those derived from unimodal data. Finally, we used partial least squares to identify relationship between hippocampus microstructure and behaviour. This work supports the use of non-negative matrix factorization as a tool for identifying spatial components in which relevant variance occurs without being constrained by existing anatomical delineations, and advocates for continued use of multimodal data when defining boundaries.

Declaration of competing interest

Authors report no conflicts of interest.

Acknowledgements

This work was supported by funding from the Fonds de Recherche du Québec Santé, CIHR, NSERC and McGill University (Shuk-Tak Liang Fellowship). RP receives salary support from the Fonds de Recherche du Québec Santé. Dr. Chakravarty receives salary support from the Fonds de Recherche du Québec Santé. We would like to thank Dr. Ragini Verma (Professor in Section of Biomedical Image Analysis, Department of Radiology, University of Pennsylvania) for her discussion and consultations regarding diffusion processing. Data were provided by the Human Connectome Project, WU-Minn Consortium (Principal Investigators: David Van Essen and Kamil Ugurbil; 1U54MH091657). Data processing was performed in part using the General Purpose Cluster resources of the SciNet HPC Consortium (Loken et al., 2010).

Appendix A. Supplementary data

Supplementary data to this article can be found online at https://doi.org/10.1016/j.neuroimage.2019.116348.

References

Adler, D.H., Wisse, L.E.M., Ittyerah, R., Pluta, J.B., Ding, S.-L., Xie, L., et al., 2018. Characterizing the human hippocampus in aging and Alzheimer's disease using a computational atlas derived from ex vivo MRI and histology. Proc. Natl. Acad. Sci. U.S.A. 115 (16), 4252–4257.

Adnan, A., Barnett, A., Moayedi, M., McCormick, C., Cohn, M., McAndrews, M.P., 2016. Distinct hippocampal functional networks revealed by tractography-based parcellation. Brain Struct. Funct. 221 (6), 2999–3012.

Alexander, A.L., Lee, J.E., Lazar, M., Field, A.S., 2007. Diffusion tensor imaging of the brain. Neurotherapeutics: The Journal of the American Society for Experimental NeuroTherapeutics 4 (3), 316–329.

Alfaro-Almagro, F., Jenkinson, M., Bangerter, N.K., Andersson, J.L.R., Griffanti, L., Douaud, G., et al., 2018. Image processing and Quality Control for the first 10,000 brain imaging datasets from UK Biobank. Neuroimage 166, 400–424.

Amaral, D.G., Scharfman, H.E., Lavenex, P., 2007. The dentate gyrus: fundamental neuroanatomical organization (dentate gyrus for dummies). Prog. Brain Res. 163, 3–22.

Amaral, R.S.C., Park, M.T.M., Devenyi, G.A., Lynn, V., Pipitone, J., Winterburn, J., et al., 2018. Manual segmentation of the fornix, fimbria, and alveus on high-resolution 3T MRI: application via fully-automated mapping of the human memory circuit white and grey matter in healthy and pathological aging. Neuroimage 170, 132–150.

Amunts, K., Kedo, O., Kindler, M., Pieperhoff, P., Mohlberg, H., Shah, N.J., et al., 2005. Cytoarchitectonic mapping of the human amygdala, hippocampal region and entorhinal cortex: intersubject variability and probability maps. Anat. Embryol. 210 (5–6), 343–352.

Andersen, P., Morris, R., Amaral, D., O'Keefe, J., Division of Neurophysiology, Bliss, T., 2007. The Hippocampus Book. Oxford University Press, USA.

Andersson, J., Xu, J., Yacoub, E., Auerbach, E., Moeller, S., Ugurbil, K., 2012. A comprehensive Gaussian process framework for correcting distortions and movements in diffusion images. Proceedings of the 20th Annual Meeting of ISMRM 2426.

Arbabshirani, M.R., Plis, S., Sui, J., Calhoun, V.D., 2017. Single subject prediction of brain disorders in neuroimaging: promises and pitfalls. Neuroimage 145 (Pt B), 137–165.

Arshad, M., Stanley, J.A., Raz, N., 2017. Test-retest reliability and concurrent validity of in vivo myelin content indices: myelin water fraction and calibrated T1 w/T2 w image ratio. Hum. Brain Mapp. 38 (4), 1780–1790.

Asperholm, M., Nagar, S., Dekhtyar, S., Herlitz, A., 2019. The magnitude of sex differences in verbal episodic memory increases with social progress: data from 54 countries across 40 years. PLoS One 14 (4), e0214945.

Avants, B.B., Epstein, C.L., Grossman, M., Gee, J.C., 2008. Symmetric diffeomorphic image registration with cross-correlation: evaluating automated labeling of elderly and neurodegenerative brain. Med. Image Anal. 12 (1), 26–41.

Avants, B.B., Yushkevich, P., Pluta, J., Minkoff, D., Korczykowski, M., Detre, J., Gee, J.C., 2010. The optimal template effect in hippocampus studies of diseased populations. Neuroimage 49 (3), 2457–2466.

Barch, D.M., Burgess, G.C., Harms, M.P., Petersen, S.E., Schlaggar, B.L., Corbetta, M., et al., 2013. Function in the human connectome: task-fMRI and individual differences in behavior. Neuroimage 80, 169–189.

Bartzokis, G., 2004. Age-related myelin breakdown: a developmental model of cognitive decline and Alzheimer's disease. Neurobiol. Aging 25 (1), 5–18.

Basser, P.J., Mattiello, J., LeBihan, D., 1994. MR diffusion tensor spectroscopy and imaging. Biophys. J. 66 (1), 259–267.

Beckmann, C.F., DeLuca, M., Devlin, J.T., Smith, S.M., 2005. Investigations into resting-state connectivity using independent component analysis. Philos. Trans. R. Soc. Lond. Ser. B Biol. Sci. 360 (1457), 1001–1013.

Beckmann, C.F., Smith, S.M., 2005. Tensorial extensions of independent component analysis for multisubject FMRI analysis. Neuroimage 25, 294–311. https://doi.org/10.1016/j.neuroimage.2004.10.043.

Beissner, F., Preibisch, C., Schweizer-Arau, A., Popovici, R.M., Meissner, K., 2018. Psychotherapy with somatosensory stimulation for endometriosis-associated pain: the role of the anterior Hippocampus. Biol. Psychiatry 84, 734–742. https://doi.org/10.1016/j.biopsych.2017.01.006.

Ben-Hur, A., Elisseeff, A., Guyon, I., 2002. A stability based method for discovering structure in clustered data. *Pacific Symposium on Biocomputing*. Pacific Symposium on Biocomputing 6–17.

Bilker, W.B., Hansen, J.A., Brensinger, C.M., Richard, J., Gur, R.E., Gur, R.C., 2012. Development of abbreviated nine-item forms of the Raven's standard progressive matrices test. Assessment 19, 354–369. https://doi.org/10.1177/1073191112446655.

Blessing, E.M., Beissner, F., Schumann, A., Brünner, F., Bär, K.-J., 2016. A data-driven approach to mapping cortical and subcortical intrinsic functional connectivity along the longitudinal hippocampal axis. Hum. Brain Mapp. 37 (2), 462–476.

Boutsidis, C., Gallopoulos, E., 2008. SVD based initialization: a head start for nonnegative matrix factorization. Pattern Recognit. 41 (4), 1350–1362.

Braak, H., Braak, E., 1991. Neuropathological stageing of Alzheimer-related changes. Acta Neuropathol. 82 (4), 239–259.

Bremner, J.D., Narayan, M., Anderson, E.R., Staib, L.H., Miller, H.L., Charney, D.S., 2000. Hippocampal volume reduction in major depression. Am. J. Psychiatry 157 (1), 115–118.

Burgess, N., Jeffery, K.J., O'Keefe, J. (Eds.), 1999. The Hippocampal and Parietal Foundations of Spatial Cognition, p. 490. Retrieved from. https://psycnet.apa.org/fulltext/1999-02910-000.pdf.

Burgess, N., Maguire, E.A., O'Keefe, J., 2002. The human hippocampus and spatial and episodic memory. Neuron 35 (4), 625–641.

Calhoun, V.D., Adali, T., Pearlson, G.D., Pekar, J.J., 2001. A method for making group inferences from functional MRI data using independent component analysis. Hum. Brain Mapp. 14 (3), 140–151.

Callaghan, M.F., Freund, P., Draganski, B., Anderson, E., Cappelletti, M., Chowdhury, R., et al., 2014. Widespread age-related differences in the human brain microstructure revealed by quantitative magnetic resonance imaging. Neurobiol. Aging 35 (8), 1862–1872.

Carlesimo, G.A., Cherubini, A., Caltagirone, C., Spalletta, G., 2010. Hippocampal mean diffusivity and memory in healthy elderly individuals: a cross-sectional study. Neurology 74 (3), 194–200.

Casey, B.J., Cannonier, T., Conley, M.I., Cohen, A.O., Barch, D.M., Heitzeg, M.M., ABCD Imaging Acquisition Workgroup, 2018. The adolescent brain cognitive development (ABCD) study: imaging acquisition across 21 sites. Developmental Cognitive Neuroscience 32, 43–54.

Chakravarty, M.M., Sadikot, A.F., Germann, J., Bertrand, G., Collins, D.L., 2008. Towards a validation of atlas warping techniques. Med. Image Anal. 12 (6), 713–726.

Chakravarty, M.M., Steadman, P., van Eede, M.C., Calcott, R.D., Gu, V., Shaw, P., et al., 2013. Performing label-fusion-based segmentation using multiple automatically generated templates. Hum. Brain Mapp. 34 (10), 2635–2654.

Charlton, R.A., Barrick, T.R., McIntyre, D.J., Shen, Y., O'Sullivan, M., Howe, F.A., et al., 2006. White matter damage on diffusion tensor imaging correlates with age-related cognitive decline. Neurology 66 (2), 217–222.
Charlton, R.A., Schiavone, F., Barrick, T.R., Morris, R.G., Markus, H.S., 2010. Diffusion tensor imaging detects age related white matter change over a 2 year follow-up which is associated with working memory decline. J. Neurol. Neurosurg. Psychiatry 81 (1), 13–19.
Chase, H.W., Clos, M., Dibble, S., Fox, P., Grace, A.A., Phillips, M.L., Eickhoff, S.B., 2015. Evidence for an anterior-posterior differentiation in the human hippocampal formation revealed by meta-analytic parcellation of fMRI coordinate maps: focus on the subiculum. Neuroimage 113, 44–60.
Crane, J., Milner, B., 2005. What went where? Impaired object-location learning in patients with right hippocampal lesions. Hippocampus 15 (2), 216–231.
de Flores, R., La Joie, R., Chételat, G., 2015. Structural imaging of hippocampal subfields in healthy aging and Alzheimer's disease. Neuroscience 309, 29–50.
den Heijer, T., der Lijn, van, F., Vernooij, M.W., de Groot, M., Koudstaal, P.J., van der Lugt, A., et al., 2012. Structural and diffusion MRI measures of the hippocampus and memory performance. Neuroimage 63 (4), 1782–1789.
de Wit, H., Flory, J.D., Acheson, A., McCloskey, M., Manuck, S.B., 2007. IQ and nonplanning impulsivity are independently associated with delay discounting in middle-aged adults. Personal. Individ. Differ. 42 (1), 111–121.
Dickerson, B.C., Eichenbaum, H., 2009. The Episodic Memory System: Neurocircuitry and Disorders, vol. 35. Neuropsychopharmacology: Official Publication of the American College of Neuropsychopharmacology, p. 86.
Durran, D.R., 2013. Numerical Methods for Wave Equations in Geophysical Fluid Dynamics. Springer Science & Business Media.
Duvernoy, H.M., Bourgouin, P., 1998. The Human hippocampus : Functional Anatomy, Vascularization and Serial Sections with MRI. Springer, Berlin; New York.
Eickhoff, S.B., Yeo, B.T.T., Genon, S., 2018. Imaging-based parcellations of the human brain. Nat. Rev. Neurosci. 19 (11), 672–686.
Erickson, K.I., Voss, M.W., Prakash, R.S., Basak, C., Szabo, A., Chaddock, L., et al., 2011. Exercise training increases size of hippocampus and improves memory. Proc. Natl. Acad. Sci. U.S.A. 108 (7), 3017–3022.
Ezzati, A., Katz, M.J., Zammit, A.R., Lipton, M.L., Zimmerman, M.E., Sliwinski, M.J., Lipton, R.B., 2016. Differential association of left and right hippocampal volumes with verbal episodic and spatial memory in older adults. Neuropsychologia 93 (Pt B), 380–385.
Fletcher, P.C., Frith, C.D., Rugg, M.D., 1997. The functional neuroanatomy of episodic memory. Trends Neurosci. 20, 213–218. https://doi.org/10.1016/s0166-2236(96)01013-2.
Fornberg, B., 1988. Generation of finite difference formulas on arbitrarily spaced grids. Math. Comput. 51 (184), 699–706.
Fotuhi, M., Do, D., Jack, C., 2012. Modifiable factors that alter the size of the hippocampus with ageing. Nat. Rev. Neurol. 8 (4), 189–202.
Ganzetti, M., Wenderoth, N., Mantini, D., 2014. Whole brain myelin mapping using T1- and T2-weighted MR imaging data. Front. Hum. Neurosci. 8 (September), 671.
Ge, R., Kot, P., Liu, X., Lang, D.J., Wang, J.Z., Honer, W.G., Vila-Rodriguez, F., 2019. Parcellation of the human hippocampus based on gray matter volume covariance: Replicable results on healthy young adults. *Human Brain Mapping*. https://doi.org/10.1002/hbm.24628.
Glasser, M.F., Coalson, T.S., Robinson, E.C., Hacker, C.D., Harwell, J., Yacoub, E., et al., 2016. A multi-modal parcellation of human cerebral cortex. Nature 536 (7615), 171–178.
Glasser, M.F., Sotiropoulos, S.N., Wilson, J.A., Coalson, T.S., Fischl, B., Andersson, J.L., et al., 2013. The minimal preprocessing pipelines for the Human Connectome Project. Neuroimage 80, 105–124.
Glasser, M.F., Van Essen, D.C., 2011. Mapping human cortical areas in vivo based on myelin content as revealed by T1- and T2-weighted MRI. J. Neurosci.: The Official Journal of the Society for Neuroscience 31 (32), 11597–11616.
Grydeland, H., Walhovd, K.B., Tamnes, C.K., Westlye, L.T., Fjell, A.M., 2013. Intracortical myelin links with performance variability across the human lifespan: results from T1- and T2-weighted MRI myelin mapping and diffusion tensor imaging. J. Neurosci.: The Official Journal of the Society for Neuroscience 33 (47), 18618–18630.
Gur, R.C., Alsop, D., Glahn, D., Petty, R., Swanson, C.L., Maldjian, J.A., et al., 2000. An fMRI study of sex differences in regional activation to a verbal and a spatial task. Brain Lang. 74 (2), 157–170.
Gur, R.C., Gur, R.E., Obrist, W.D., Hungerbuhler, J.P., Younkin, D., Rosen, A.D., et al., 1982. Sex and handedness differences in cerebral blood flow during rest and cognitive activity. Science 217 (4560), 659–661.
Gur, R.C., Richard, J., Calkins, M.E., Chiavacci, R., Hansen, J.A., Bilker, W.B., et al., 2012. Age group and sex differences in performance on a computerized neurocognitive battery in children age 8−21. Neuropsychology 26, 251–265. https://doi.org/10.1037/a0026712.
Gur, R.C., Richard, J., Hughett, P., Calkins, M.E., Macy, L., Bilker, W.B., et al., 2010. A cognitive neuroscience-based computerized battery for efficient measurement of individual differences: standardization and initial construct validation. J. Neurosci. Methods 187 (2), 254–262.
Halko, N., Martinsson, P., Tropp, J., 2011. Finding structure with Randomness: probabilistic algorithms for constructing approximate matrix decompositions. SIAM Rev. 53 (2), 217–288.
Hansen, L.K., Larsen, J., Nielsen, F.A., Strother, S.C., Rostrup, E., Savoy, R., et al., 1999. Generalizable patterns in neuroimaging: how many principal components? Neuroimage 9 (5), 534–544.
Heckers, S., 2001. Neuroimaging studies of the hippocampus in schizophrenia. Hippocampus 11 (5), 520–528.
Iturria-Medina, Y., Carbonell, F.M., Sotero, R.C., Chouinard-Decorte, F., Evans, A.C., Alzheimer's Disease Neuroimaging Initiative, 2017. Multifactorial causal model of brain (dis)organization and therapeutic intervention: application to Alzheimer's disease. Neuroimage 152, 60–77.
Jack Jr., C.R., Petersen, R.C., Xu, Y.C., O'Brien, P.C., Smith, G.E., Ivnik, R.J., et al., 1999. Prediction of AD with MRI-based hippocampal volume in mild cognitive impairment. Neurology 52 (7), 1397–1403.
Jernigan, T.L., Brown, S.A., ABCD Consortium Coordinators, 2018. Introduction. Developmental Cognitive Neuroscience 32, 1–3.
Jones, D.K., Basser, P.J., 2004. "Squashing peanuts and smashing pumpkins": how noise distorts diffusion-weighted MR data. Magn. Reson. Med.: Official Journal of the Society of Magnetic Resonance in Medicine / Society of Magnetic Resonance in Medicine 52 (5), 979–993.
Jones, D.K., Knösche, T.R., Turner, R., 2013. White matter integrity, fiber count, and other fallacies: the do's and don'ts of diffusion MRI. Neuroimage 73, 239–254.
Kaufman, A.S., Kaufman, J.C., Liu, X., Johnson, C.K., 2009. How do educational attainment and gender relate to fluid intelligence, crystallized intelligence, and academic skills at ages 22-90 years? Arch. Clin. Neuropsychol.: The Official Journal of the National Academy of Neuropsychologists 24 (2), 153–163.
Khan, A.R., Wang, L., Beg, M.F., 2008. FreeSurfer-initiated fully-automated subcortical brain segmentation in MRI using large deformation diffeomorphic metric mapping. Neuroimage 41 (3), 735–746.
Kharabian Masouleh, S., Eickhoff, S.B., Hoffstaedter, F., Genon, S., Alzheimer's Disease Neuroimaging Initiative, 2019. Empirical examination of the replicability of associations between brain structure and psychological variables. eLife 8. https://doi.org/10.7554/eLife.43464.
Kochunov, P., Williamson, D.E., Lancaster, J., Fox, P., Cornell, J., Blangero, J., Glahn, D.C., 2012. Fractional anisotropy of water diffusion in cerebral white matter across the lifespan. Neurobiol. Aging 33 (1), 9–20.
Krishnan, A., Williams, L.J., McIntosh, A.R., Abdi, H., 2011. Partial Least Squares (PLS) methods for neuroimaging: a tutorial and review. Neuroimage 56 (2), 455–475.
Lebel, C., Gee, M., Camicioli, R., Wieler, M., Martin, W., Beaulieu, C., 2012. Diffusion tensor imaging of white matter tract evolution over the lifespan. Neuroimage 60 (1), 340–352.
Lebel, C., Walker, L., Leemans, A., Phillips, L., Beaulieu, C., 2008. Microstructural maturation of the human brain from childhood to adulthood. Neuroimage 40 (3), 1044–1055.
Lebreton, M., Bertoux, M., Boutet, C., Lehericy, S., Dubois, B., Fossati, P., Pessiglione, M., 2013. A critical role for the hippocampus in the valuation of imagined outcomes. PLoS Biol. 11 (10), e1001684.
Lee, D.D., Seung, H.S., 1999. Learning the parts of objects by non-negative matrix factorization. Nature 401 (6755), 788–791.
Liem, F., Varoquaux, G., Kynast, J., Beyer, F., Kharabian Masouleh, S., Huntenburg, J.M., et al., 2017. Predicting brain-age from multimodal imaging data captures cognitive impairment. Neuroimage 148, 179–188.
Loken, C., Gruner, D., Groer, L., Peltier, R., Bunn, N., Craig, M., et al., 2010. SciNet: lessons learned from building a power-efficient top-20 system and data centre. J. Phys. Conf. Ser. 256 (1), 012026.
Marner, L., Nyengaard, J.R., Tang, Y., Pakkenberg, B., 2003. Marked loss of myelinated nerve fibers in the human brain with age. J. Comp. Neurol. 462 (2), 144–152.
McIntosh, A.R., Lobaugh, N.J., 2004. Partial least squares analysis of neuroimaging data: applications and advances. Neuroimage 23 (Suppl. 1), S250–S263.
McIntosh, A.R., Mišić, B., 2013. Multivariate statistical analyses for neuroimaging data. Annu. Rev. Psychol. 64, 499–525.
Mielke, M.M., Okonkwo, O.C., Oishi, K., Mori, S., Tighe, S., Miller, M.I., et al., 2012. Fornix integrity and hippocampal volume predict memory decline and progression to Alzheimer's disease. Alzheimer's Dementia: The Journal of the Alzheimer's Association 8 (2), 105–113.
Miller, K.L., Alfaro-Almagro, F., Bangerter, N.K., Thomas, D.L., Yacoub, E., Xu, J., et al., 2016. Multimodal population brain imaging in the UK Biobank prospective epidemiological study. Nat. Neurosci. 19 (11), 1523–1536.
Müller, M.J., Greverus, D., Weibrich, C., Dellani, P.R., Scheurich, A., Stoeter, P., Fellgiebel, A., 2007. Diagnostic utility of hippocampal size and mean diffusivity in amnestic MCI. Neurobiol. Aging 28 (3), 398–403.
Narr, K.L., Thompson, P.M., Szeszko, P., Robinson, D., Jang, S., Woods, R.P., et al., 2004. Regional specificity of hippocampal volume reductions in first-episode schizophrenia. Neuroimage 21 (4), 1563–1575.
Nassar, R., Kaczkurkin, A.N., Xia, C.H., Sotiras, A., Pehlivanova, M., Moore, T.M., et al., 2018. Gestational age is dimensionally associated with structural brain network abnormalities across development. Cerebral Cortex. https://doi.org/10.1093/cercor/bhy091.
Nazeri, A., Chakravarty, M.M., Rotenberg, D.J., Rajji, T.K., Rathi, Y., Michailovich, O.V., Voineskos, A.N., 2015. Functional consequences of neurite orientation dispersion and density in humans across the adult lifespan. J. Neurosci.: The Official Journal of the Society for Neuroscience 35 (4), 1753–1762.
Nordin, K., Persson, J., Stening, E., Herlitz, A., Larsson, E.-M., Söderlund, H., 2018. Structural whole-brain covariance of the anterior and posterior hippocampus: associations with age and memory. Hippocampus 28 (2), 151–163.
Nyberg, L., McIntosh, A.R., Cabeza, R., Habib, R., Houle, S., Tulving, E., 1996. General and specific brain regions involved in encoding and retrieval of events: what, where, and when. Proc. Natl. Acad. Sci. U.S.A. 93 (20), 11280–11285.
O'Keefe, J., Dostrovsky, J., 1971. The hippocampus as a spatial map. Preliminary evidence from unit activity in the freely-moving rat. Brain Res. 34 (1), 171–175.
O'Shea, A., Cohen, R.A., Porges, E.C., Nissim, N.R., Woods, A.J., 2016. Cognitive aging and the Hippocampus in older adults. Front. Aging Neurosci. 8, 298.

Papp, K.V., Kaplan, R.F., Springate, B., Moscufo, N., Wakefield, D.B., Guttmann, C.R.G., Wolfson, L., 2014. Processing speed in normal aging: effects of white matter hyperintensities and hippocampal volume loss. Neuropsychology, Development, and Cognition. Section B, Aging, Neuropsychology and Cognition 21 (2), 197–213.
Patel, S., Park, M.T.M., Devenyi, G.A., Patel, R., Masellis, M., Knight, J., Chakravarty, M.M., 2017. Heritability of hippocampal subfield volumes using a twin and non-twin siblings design. Hum. Brain Mapp. 38 (9), 4337–4352.
Persson, J., Spreng, R.N., Turner, G., Herlitz, A., Morell, A., Stening, E., et al., 2014. Sex differences in volume and structural covariance of the anterior and posterior hippocampus. Neuroimage 99, 215–225.
Peters, J., Büchel, C., 2010. Episodic future thinking reduces reward delay discounting through an enhancement of prefrontal-mediotemporal interactions. Neuron 66 (1), 138–148.
Pipitone, J., Park, M.T.M., Winterburn, J., Lett, T.A., Lerch, J.P., Pruessner, J.C., et al., 2014. Multi-atlas segmentation of the whole hippocampus and subfields using multiple automatically generated templates. Neuroimage 101, 494–512.
Plachti, A., Eickhoff, S.B., Hoffstaedter, F., Patil, K.R., Laird, A.R., Fox, P.T., et al., 2019. Multimodal parcellations and extensive behavioral profiling tackling the Hippocampus gradient. Cerebr. Cortex. https://doi.org/10.1093/cercor/bhy336.
Résolution des équations et des systèmes non linéaires. In: Quarteroni, A., Sacco, R., Saleri, F. (Eds.), 2007. Méthodes Numériques: Algorithmes, analyse et applications. Springer Milan, Milano, pp. 211–257.
Reimers, S., Maylor, E.A., Stewart, N., Chater, N., 2009. Associations between a one-shot delay discounting measure and age, income, education and real-world impulsive behavior. Personal. Individ. Differ. 47 (8), 973–978.
Reuben, A., Brickman, A.M., Muraskin, J., Steffener, J., Stern, Y., 2011. Hippocampal atrophy relates to fluid intelligence decline in the elderly. J. Int. Neuropsychol. Soc.: JINS 17 (1), 56–61.
Robinson, J.L., Salibi, N., Deshpande, G., 2016. Functional connectivity of the left and right hippocampi: evidence for functional lateralization along the long-axis using meta-analytic approaches and ultra-high field functional neuroimaging. Neuroimage 135, 64–78.
Sabuncu, M.R., Desikan, R.S., Sepulcre, J., Yeo, B.T.T., Liu, H., Schmansky, N.J., et al., 2011. The dynamics of cortical and hippocampal atrophy in Alzheimer disease. Arch. Neurol. 68 (8), 1040–1048.
Sankar, T., Park, M.T.M., Jawa, T., Patel, R., Bhagwat, N., Voineskos, A.N., et al., 2017. Your algorithm might think the hippocampus grows in Alzheimer's disease: caveats of longitudinal automated hippocampal volumetry. Hum. Brain Mapp. 38 (6), 2875–2896.
Schiavone, F., Charlton, R.A., Barrick, T.R., Morris, R.G., Markus, H.S., 2009. Imaging age-related cognitive decline: a comparison of diffusion tensor and magnetization transfer MRI. J. Magn. Reson. Imaging: JMRI 29 (1), 23–30.
Scott, J.A., Tosun, D., Braskie, M.N., Maillard, P., Thompson, P.M., Weiner, M., et al., 2017. Independent value added by diffusion MRI for prediction of cognitive function in older adults. NeuroImage. Clinical 14, 166–173.
Shafee, R., Buckner, R.L., Fischl, B., 2015. Gray matter myelination of 1555 human brains using partial volume corrected MRI images. Neuroimage 105, 473–485.
Small, S.A., 2002. The longitudinal axis of the hippocampal formation: its anatomy, circuitry, and role in cognitive function. Rev. Neurosci. 13 (2), 183–194.
Small, S.A., Schobel, S.A., Buxton, R.B., Witter, M.P., Barnes, C.A., 2011. A pathophysiological framework of hippocampal dysfunction in ageing and disease. Nat. Rev. Neurosci. 12 (10), 585–601.
Sotiras, A., Resnick, S.M., Davatzikos, C., 2015. Finding imaging patterns of structural covariance via Non-Negative Matrix Factorization. Neuroimage 108, 1–16.
Sotiras, A., Toledo, J.B., Gur, R.E., Gur, R.C., Satterthwaite, T.D., Davatzikos, C., 2017. Patterns of coordinated cortical remodeling during adolescence and their associations with functional specialization and evolutionary expansion. Proc. Natl. Acad. Sci. U.S.A. 114 (13), 3527–3532.
Sotiropoulos, S.N., Jbabdi, S., Xu, J., Andersson, J.L., Moeller, S., Auerbach, E.J., et al., 2013. Advances in diffusion MRI acquisition and processing in the human connectome Project. Neuroimage 80, 125–143.
Strange, B.A., Witter, M.P., Lein, E.S., Moser, E.I., 2014. Functional organization of the hippocampal longitudinal axis. Nat. Rev. Neurosci. 15 (10), 655–669.
Tardif, C.L., Gauthier, C.J., Steele, C.J., Bazin, P.-L., Schäfer, A., Schaefer, A., et al., 2016. Advanced MRI techniques to improve our understanding of experience-induced neuroplasticity. Neuroimage 131, 55–72.
Terry, D.P., Sabatinelli, D., Nicolas, P.A., Lazar, N.A., Miller, S.L., 2015. A meta-analysis of fMRI activation differences during episodic memory in Alzheimer's disease and mild cognitive impairment. J. Neuroimaging: Official Journal of the American Society of Neuroimaging 25 (6), 849–860.
Thompson, C.L., Pathak, S.D., Jeromin, A., Ng, L.L., MacPherson, C.R., Mortrud, M.T., et al., 2008. Genomic anatomy of the Hippocampus. Neuron 60 (6), 1010–1021.
Tournier, J.-D., Calamante, F., Connelly, A., 2012. MRtrix: diffusion tractography in crossing fiber regions. Int. J. Imaging Syst. Technol. 22 (1), 53–66.
Tournier, J.-D., Mori, S., Leemans, A., 2011. Diffusion tensor imaging and beyond. Magn. Reson. Med.: Official Journal of the Society of Magnetic Resonance in Medicine / Society of Magnetic Resonance in Medicine 65 (6), 1532–1556.
Tullo, S., Patel, R., Devenyi, G.A., et al., 2019. MR-based age-related effects on the striatum, globus pallidus, and thalamus in healthy individuals across the adult lifespan. Hum Brain Mapp 40, 5269–5288. https://doi.org/10.1002/hbm.24771.
Tulving, E., Markowitsch, H.J., 1998. Episodic and declarative memory: role of the hippocampus. Hippocampus 8 (3), 198–204.
Uddin, M.N., Figley, T.D., Marrie, R.A., Figley, C.R., CCOMS Study Group, 2018. Can T1 w/T2 w ratio be used as a myelin-specific measure in subcortical structures? Comparisons between FSE-based T1 w/T2 w ratios, GRASE-based T1 w/T2 w ratios and multi-echo GRASE-based myelin water fractions. NMR Biomed. 31 (3) https://doi.org/10.1002/nbm.3868.
Uğurbil, K., Xu, J., Auerbach, E.J., Moeller, S., Vu, A.T., Duarte-Carvajalino, J.M., et al., 2013. Pushing spatial and temporal resolution for functional and diffusion MRI in the Human Connectome Project. Neuroimage 80, 80–104.
van der Linden, D., Dunkel, C.S., Madison, G., 2017. Sex differences in brain size and general intelligence (g). Intelligence 63, 78–88.
Van Essen, D.C., Smith, S.M., Barch, D.M., Behrens, T.E.J., Yacoub, E., Ugurbil, K., WU-Minn HCP Consortium, 2013. The Wu-minn human connectome Project: an overview. Neuroimage 80, 62–79.
Van Essen, D.C., Ugurbil, K., Auerbach, E., Barch, D., Behrens, T.E.J., Bucholz, R., et al., 2012. The Human Connectome Project: a data acquisition perspective. Neuroimage 62 (4), 2222–2231.
van Uden, I.W.M., Tuladhar, A.M., van der Holst, H.M., van Leijsen, E.M.C., van Norden, A.G.W., de Laat, K.F., et al., 2016. Diffusion tensor imaging of the hippocampus predicts the risk of dementia; the RUN DMC study. Hum. Brain Mapp. 37 (1), 327–337.
Varikuti, D.P., Genon, S., Sotiras, A., Schwender, H., Hoffstaedter, F., Patil, K.R., et al., 2018. Evaluation of non-negative matrix factorization of grey matter in age prediction. Neuroimage 173, 394–410.
Veraart, J., Sijbers, J., Sunaert, S., Leemans, A., Jeurissen, B., 2013. Weighted linear least squares estimation of diffusion MRI parameters: strengths, limitations, and pitfalls. Neuroimage 81, 335–346.
Voineskos, A.N., Winterburn, J.L., Felsky, D., Pipitone, J., Rajji, T.K., Mulsant, B.H., Chakravarty, M.M., 2015. Hippocampal (subfield) volume and shape in relation to cognitive performance across the adult lifespan. Hum. Brain Mapp. 36 (8), 3020–3037.
Vythilingam, M., Vermetten, E., Anderson, G.M., Luckenbaugh, D., Anderson, E.R., Snow, J., et al., 2004. Hippocampal volume, memory, and cortisol status in major depressive disorder: effects of treatment. Biol. Psychiatry vol. 56 (2), 101–112.
Westin, C.-F., Peled, S., Gudbjartsson, H., Kikinis, R., Jolesz, F.A., 1997. Geometrical diffusion measures for MRI from tensor basis analysis. ISMRM '97, 1742 (Vancouver Canada).
Whelan, C.D., Hibar, D.P., van Velzen, L.S., Zannas, A.S., Carrillo-Roa, T., McMahon, K., et al., 2016. Heritability and reliability of automatically segmented human hippocampal formation subregions. Neuroimage 128, 125–137.
Winterburn, J.L., Pruessner, J.C., Chavez, S., Schira, M.M., Lobaugh, N.J., Voineskos, A.N., Chakravarty, M.M., 2013. A novel in vivo atlas of human hippocampal subfields using high-resolution 3 T magnetic resonance imaging. Neuroimage 74, 254–265.
Wisse, L.E.M., Biessels, G.J., Heringa, S.M., Kuijf, H.J., Koek, D.H.L., Luijten, P.R., et al., 2014. Hippocampal subfield volumes at 7T in early Alzheimer's disease and normal aging. Neurobiol. Aging 35 (9), 2039–2045.
Wisse, L.E.M., Daugherty, A.M., Olsen, R.K., Berron, D., Carr, V.A., Stark, C.E.L., et al., 2017. A harmonized segmentation protocol for hippocampal and parahippocampal subregions: why do we need one and what are the key goals? Hippocampus 27 (1), 3–11.
Wolf, D., Fischer, F.U., de Flores, R., Chételat, G., Fellgiebel, A., 2015. Differential associations of age with volume and microstructure of hippocampal subfields in healthy older adults. Hum. Brain Mapp. 36 (10), 3819–3831.
Yang, Z., Oja, E., 2010. Linear and nonlinear projective nonnegative matrix factorization. IEEE Trans. Neural Netw./a Publication of the IEEE Neural Networks Council 21 (5), 734–749.
Yushkevich, P.A., Amaral, R.S.C., Augustinack, J.C., Bender, A.R., Bernstein, J.D., Boccardi, M., et al., 2015a. Quantitative comparison of 21 protocols for labeling hippocampal subfields and parahippocampal subregions in in vivo MRI: towards a harmonized segmentation protocol. Neuroimage 111, 526–541.
Yushkevich, P.A., Pluta, J.B., Wang, H., Xie, L., Ding, S.-L., Gertje, E.C., et al., 2015b. Automated volumetry and regional thickness analysis of hippocampal subfields and medial temporal cortical structures in mild cognitive impairment. Hum. Brain Mapp. 36 (1), 258–287.
Yushkevich, P.A., Wang, H., Pluta, J., Das, S.R., Craige, C., Avants, B.B., et al., 2010. Nearly automatic segmentation of hippocampal subfields in in vivo focal T2-weighted MRI. Neuroimage 53 (4), 1208–1224.
Zatorre, R.J., Fields, R.D., Johansen-Berg, H., 2012. Plasticity in gray and white: neuroimaging changes in brain structure during learning. Nat. Neurosci. 15 (4), 528–536.
Zeighami, Y., Fereshtehnejad, S.-M., Dadar, M., Collins, D.L., Postuma, R.B., Mišić, B., Dagher, A., 2017. A clinical-anatomical signature of Parkinson's disease identified with partial least squares and magnetic resonance imaging. Neuroimage. https://doi.org/10.1016/j.neuroimage.2017.12.050.
Zeineh, M.M., Palomero-Gallagher, N., Axer, M., Gräßel, D., Goubran, M., Wree, A., et al., 2017. Direct visualization and mapping of the spatial course of fiber tracts at microscopic resolution in the human Hippocampus. Cerebr. Cortex 27 (3), 1779–1794.
Zhao, R., Zhang, X., Zhu, Y., Fei, N., Sun, J., Liu, P., et al., 2019. Disrupted resting-state functional connectivity in hippocampal subregions after sleep deprivation. Neuroscience 398, 37–54.
Zhu, B., Chen, C., Dang, X., Dong, Q., Lin, C., 2017. Hippocampal subfields' volumes are more relevant to fluid intelligence than verbal working memory. Intelligence 61, 169–175.